Characterization of scintillators for nuclear fusion reactors

Eduardo Nieto Vargas
July 2023

Bachelor Thesis
Degree in Physics

Supervisor:
Joaquín Galdón Quiroga

Faculty of Physics
Department of Atomic, Molecular and Nuclear Physics
University of Sevilla
Spain

Abstract

Nuclear fusion is considered nowadays as the most promising energy source in the long term. Magnetic confinement reactors, like the tokamak, are the most developed models, inside which plasma is confined. Diagnostics in these reactors are necessary to understand the plasma properties, and some of them use scintillators as active component. Therefore, they must be well characterized in order to choose the most suitable material for each diagnostic. In this context, a series of experiments were carried out in the CNA (*Centro Nacional de Aceleradores*), at Sevilla. They consisted in the irradiation of scintillators with energetic ions of ^{7}Li and ^{51}V, with energies from 1 to 3 MeV. The chosen scintillators were TG-Green, CSO, TCH, ZnS, YAG and YAGGd. Three aspects of the scintillators were characterized: linearity of emission rate with incident current; energy scan of light yield; and degradation.

In the experiments, all the materials presented linearity between emission rate and incident current. On the energy scan, ZnS presented the highest light yield, followed by TG-Green, CSO, YAGGd, YAG and TCH. TCH was also the slowest degrading scintillator, while ZnS was the fastest one. The degradation results were fitted to Black Birk's model, where a difference of two orders of magnitude was observed for the fluence of 50% ($F_{1/2}$) between lithium and vanadium. The light yield results of the energy scan were also fitted to Birk's model, where the experimental results with ^{7}Li showed the predicted linearity with energy for the high stopping power limit. TCH stood out as a low degrading material with a high linear response, despite its low light yield. This recently developed material might be then considered for diagnostics like the Imaging Heavy Ion Beam Probe.

Contents

1 Introduction

1.1 Fusion

The search of new energy sources is one of the most relevant issues nowadays, since energy consumption increases significantly while the global population grows. The traditional sources, mostly fossil resources, do not seem doable any more, due to its impact in the environment and limited availability. In this context, fusion reactors look like one of the best options to focus on [1]. Fusion reactions release nearly four million times more energy than burning coal or gas, so it has a much higher production capacity in the long term. In most relevant fusion experiments, the reagents of the fusion reaction are deuterium and tritium. Deuterium can be distilled from all forms of water, while tritium will be produced during the fusion reaction as fusion neutrons interact with lithium (sea-based reserves of lithium, used in a fusion reactor in its Li-6 isotope form, would fulfil needs for millions of years). Therefore, fusion reactors would be able to provide energy for much longer than fossil resources. Besides, fusion reactors produce neither greenhouse gases like CO_2 (the main product is helium) nor long-lived radioactive waste, making it more environmentally-friendly.
In fusion processes, two nuclei react to form a heavier nucleus. One example is the deuterium-tritium reaction, shown in Figure 1:

$$D + T \Rightarrow {}^4\mathrm{He}(3.52\ \mathrm{MeV}) + n(14.06\ \mathrm{MeV})$$

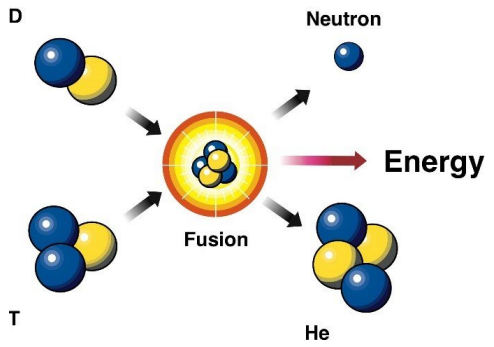

Figure 1: Deuterium-tritium fusion reaction [2]

In these reactions, energy is released as kinetic energy of the resulting nuclei. The amount of energy either produced or needed in the reaction is quantified by the reaction *Q value*, which is defined as the difference between the rest mass of the products and reactants:

$$Q = \sum_i m_i c^2 - \sum_f m_f c^2 = \sum_f B_f - \sum_i B_i, \tag{1}$$

where B is the binding energy. If the Q value is positive, the reaction is spontaneous and liberates energy. On the other hand, if it is negative, it requires additional energy to

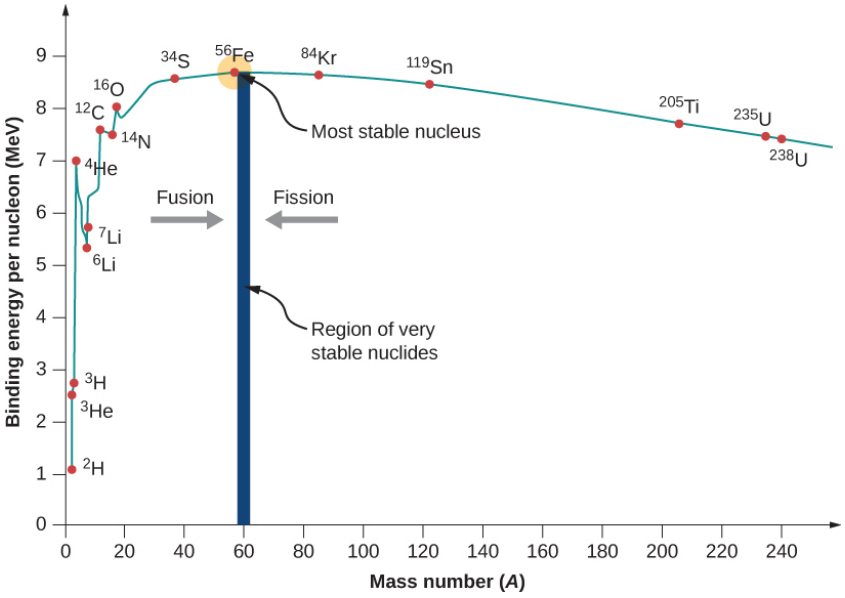

Figure 2: Binding energy of nuclei per mass number [3]

happen. Hence, processes where nuclei transform into more bound nuclei are energetically favourable and liberate energy, which can be exploited. Binding energies per nucleon can be estimated experimentally, as those shown in figure 2. The most bound nucleus per nucleon is iron. Nuclei lighter than iron tend to react to create heavier nuclei (fusion), while heavier nuclei do the opposite (fission). It can be also observed that, in the case of the deuterium-tritium reaction explained above, the difference of binding energy per nucleon from the product (helium) is significantly higher than other possibilities, being this the reason why this reaction is favoured in the design of fusion reactors, among others.

However, there is a technical problem with fusion reactions. They are ruled by the strong interaction, which has an extremely low range (around 1 fm). On the other hand, nuclei have positive charge, so they feel electric repulsion. Hence, for a fusion reaction to happen, nuclei must get close enough, so the strong interaction overcomes the coulomb repulsion. Depending on the mechanism used to give nuclei enough energy to achieve this, there exist mainly two different types of fusion reactors:

1. Inertial confinement [4]: with this technique, a small spherical target is subjected to high-powered lasers during a small interval of time ($\tau \approx 10^{-11}$ s). The target is normally composed by tritium and deuterium (it depends on the specific fusion reaction of interest) and implodes due to the large compression caused by the lasers, liberating the energy. This technique is developed mainly at the National Ignition Facility, in the USA [5].

2. Magnetic confinement [4]: it is based on the application of strong magnetic fields to confine a plasma. Plasma is an ionized gas, conformed by ions and electrons, which

are charged particles. Charged particles fulfil Lorentz's law and follow magnetic lines, circling around them. Hence, the magnetic fields make the particles of the plasma follow predictable paths and thus confines it. The plasma is heated to give the particles enough kinetic energy to overcome the Coulomb barrier. The plasma density in this type of reactor is low (around 10^{20} particles per m^3, lower than atmospheric air). In order to overcome the Coulomb barrier, temperatures of tens of keV are needed for confinement times much longer than those handled in inertial confinement (in the order of seconds). This is the reason why confinement is done by magnetic fields in the first place [6].

There are mainly two type of fusion reactors based on this technique: tokamak and stellarator. Both reactors are based on a toroidal plasma confinement system, but they differ in the way stability is achieved in the plasma [7]:

(a) In tokamak reactors, [8], a toroidal current is induced in the plasma by a transformer in the symmetry axis, which produces a poloidal magnetic field that twist the plasma. Since the current in the transformer must increase constantly, the tokamak is a pulsed device. An example of tokamak reactor is ITER, in France [8].

(b) In stellarators, no current is induced, but the plasma is completely confined by the magnetic field created by external coils. Since there is no need of inductive plasma current, it is not a pulsed device, like the tokamak. However, the toroid must now be asymmetric in order to confine efficiently the plasma. One example of stellarator prototype is the Wendelstein 7-X, in Germany [9].

The basic design of these two type of reactors is shown in figure 3. Nowadays, tokamak reactors have developed more rapidly due to their simpler design and it is established as the most promising model. For this reason, we will focus on tokamak reactors in this work.

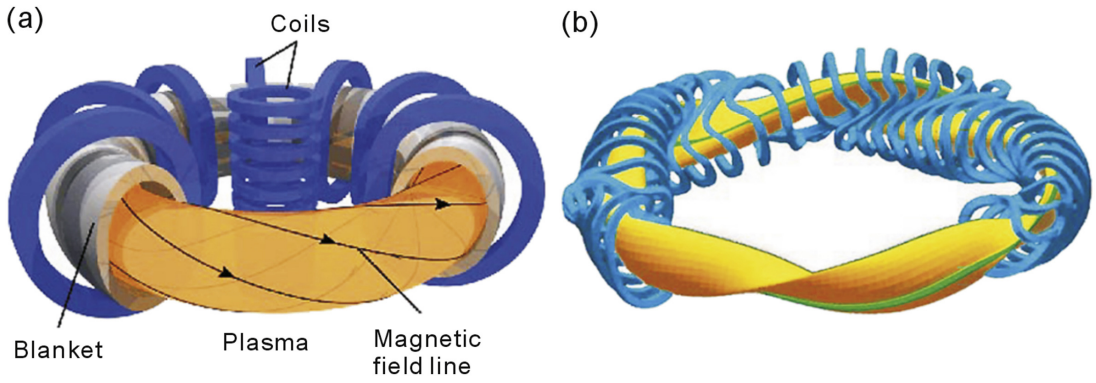

Figure 3: Design of a tokamak reactor (a) and a stellarator reactor (b) [7]

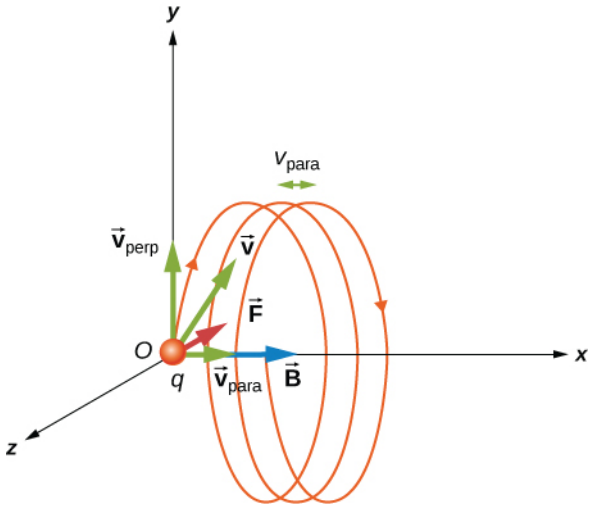

Figure 4: Trajectory of a charged particle within a magnetic field region [10]

1.2 Magnetic confinement fusion dynamics

Tokamak reactors confine plasma with charged particles using toroidal magnetic fields. These charged particles are ions and electrons. If this plasma is hot enough, the charges will gain enough kinetic energy to surpass the coulomb barrier and make fusion possible. First, we must understand how charges move when affected by a magnetic field. The force $\vec{F}$ acting on a particle with charge q due to an electric and magnetic field $\vec{E}$ and $\vec{B}$ is ruled by Lorentz's law:

$$\vec{F} = q(\vec{v} \times \vec{B} + \vec{E}). \tag{2}$$

In the case where only the magnetic field remains, the force is normal to the velocity vector of the particle, so its kinetic energy remains constant. The resulting movement of the particle is composed of the velocity component normal to the magnetic line, moving in circles normal to the magnetic lines, and the velocity component parallel to the magnetic line. In summary, the particle follows a helical trajectory, as that shown in figure 4. There are two parameters relevant for us that characterize this motion. They are the radius of the circle (Larmor's radius ρ_L) and the frequency of the movement (gyrotron frequency ω_g), which are estimated as follows:

$$\rho_L = \frac{mv_\perp}{|q|B} \quad \text{and} \quad \omega_g = \frac{v_\perp}{\rho_L} = \frac{|q|B}{m}, \tag{3}$$

where m is the mass of the particle and $v_\perp$ is the velocity component normal to the magnetic field. Another parameter of interest is the *pitch angle* Λ, which is the angle between the velocity vector and the magnetic line:

$$\Lambda = \frac{v_\parallel}{v}. \tag{4}$$

If we managed to obtain a uniform toroidal magnetic field, then this would be enough to explain particles motion. However, the magnetic field in a tokamak reactor is created

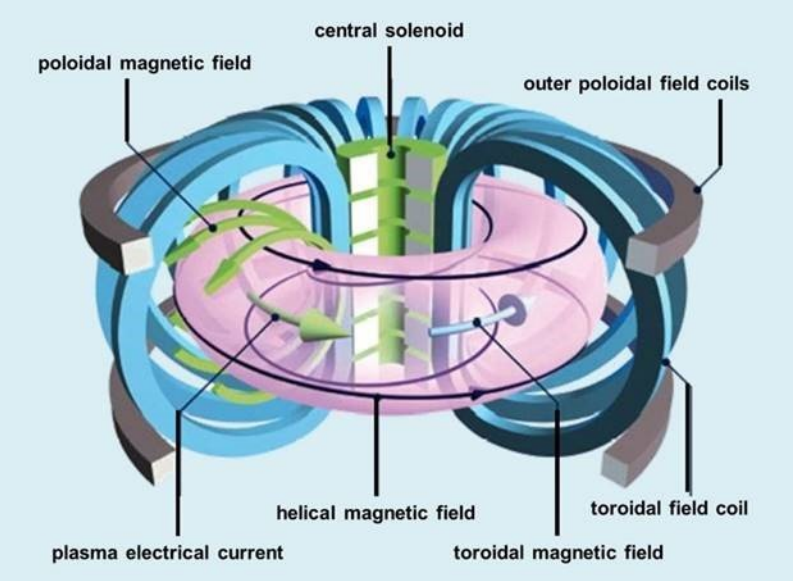

Figure 5: Schematic of tokamak-type reactor

by toroidal coils. The field produced by these coils is not constant, but has a radial dependence. This causes a vertical drift speed v_d, which sense depends on the sign of the charge. Consequently, opposite charges accumulate on opposite sides of the chamber, resulting in an electric field $\vec{E}$. This electric field also affects the charges, adding a new drift speed:

$$\vec{v}_E = \frac{\vec{E} \times \vec{B}}{||B||}.$$

The new drift speed make charges move to the walls of the chamber, making the confinement inefficient. The solution to this problem is the introduction of an additional magnetic field, normal to the toroidal one. The superposition of these two magnetic fields to make an efficient confinement of plasma is the basis of a tokamak reactor, as that shown in figure 5. The additional magnetic field is poloidal and is normally created with a transformer placed in the symmetry axis of the chamber. The transformer induces a current in the plasma, which simultaneously creates the poloidal magnetic field around it. This way, a helicoidal magnetic field that confines the plasma is achieved. Additional poloidal field coils are normally set up to make adjustments to the total magnetic field.

1.3 Scintillator based diagnostics

In a magnetic confinement fusion reactor, diagnostics are necessary to measure the plasma properties. Some of these diagnostics use scintillators, which are materials that emit photons (normally in the visible spectrum) when irradiated with ionizing radiation. Depending on the property of the plasma to be studied, there exist various diagnostics that use scintillators as detectors, which are described further below.

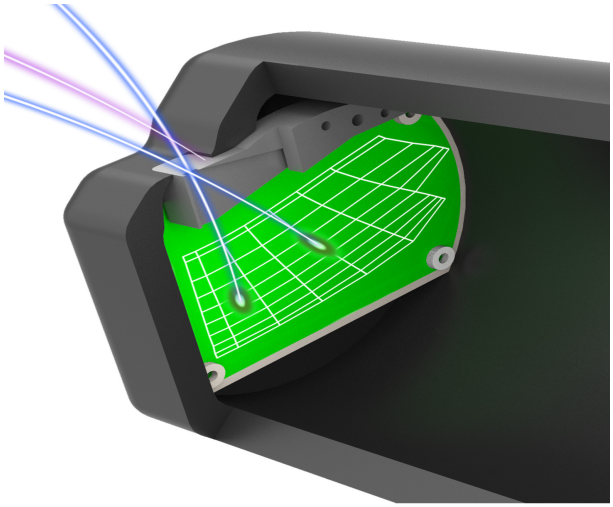

Figure 6: Fast-Ion Loss Detector (FILD): the fast ions pass through the collimator and strike the scintillator. [11]

1.3.1 Fast-Ion Loss Detectors

The plasma inside a tokamak reactor must be heated externally to reach the operation point. Despite there is a variety of heating processes, they share that a fairly large part of the total energy is transferred to the plasma bulk via fast energetic ions. Therefore, it is crucial to know the behaviour of these particles in order to understand the overall plasma dynamics.

The Fast Ion Loss Detectors diagnostic (FILD) provides information about the velocity-space of fast ions in the plasma. An example is shown in figure 6, and it works as follows: fast ions can enter the detector via a pinhole and a collimator. Once they are inside, they strike the scintillator following the trajectory determined by the magnetic lines. Then, the scintillator glows up on the hit zone and the light is recorded by a camera and a photomultiplier in the chamber. From the strike-position, the gyroradius and the pitch angle of the particle are inferred, while the photomultiplier enables a time resolved measurement.

1.3.2 Imaging Neutral Particle Analyser

In the plasma, there are both fast ions and neutral particles. Between these two particles, charge exchange can happen, where an electron is transferred from the old neutral particle to the fast ion, becoming a new neutral particle. The new neutral conserves its energy and momentum and leaves the confinement, since it is not affected by the magnetic field.

The energy and radial position of this new neutral can be measured with the Imaging Neutral Particle Analyser (INPA), as shown in figure 7. Neutral particles can access

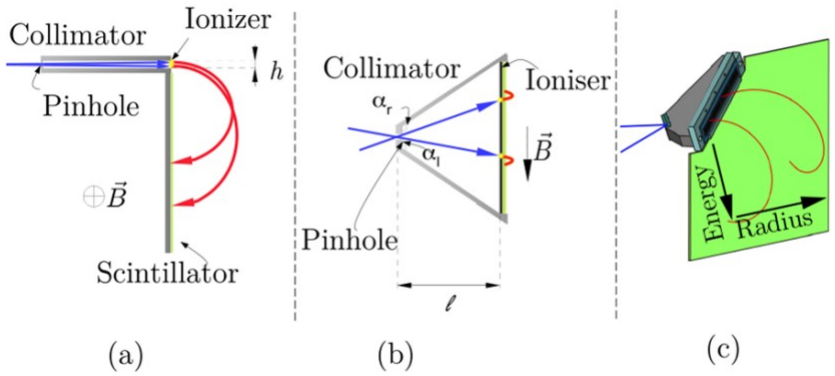

Figure 7: Imaging Neutral Particle Analyser (INPA): (a) Lateral view (b) Top view (c) 3D view [12]

the chamber of the detector through a pinhole, which leads to a collimator. Then, the neutrals reach a thin carbon foil, where they are ionized. In the detector chamber, the new ions are deviated by the magnetic field inside the reactor. A deviated ion will strike the scintillator at one point, which is recorded by a camera. The particle strike place is related to its energy, while the velocity orientation can be used to obtain the radius of the particle within the plasma.

1.3.3 Imaging Heavy Ion Beam Probe

The Imaging Heavy Ion Beam Probe diagnostic (i-HIBP) provides information about the plasma density and magnetic and electrostatic perturbations. The process is shown in figure 8 and consists in the emission of a primary beam of heavy neutral particles into the plasma. The neutrals are ionized by collisions within the plasma and then deflected by Lorentz's force, resulting in a fan of secondary beams. The secondary beams finally strike the scintillators, leaving a line-shaped trajectory. The light emitted by the scintillators is recorded by a camera. The intensity of light emitted by the scintillator depends on the density, while the location and shape of the line-shaped trajectory in the scintillator depends on the magnetic and electrostatic deviations in the plasma.

2 Scintillators

Luminescent materials are those that emit electromagnetic radiation when energy is deposited in them [6] [14]. Depending on the process by which the light is emitted, luminescence can be classified in several types: *fluorescence*, where the energy is deposited by ultraviolet or x-ray radiation; *thermoluminescence*, when light is emitted by incandescence; and *ionoluminescence*, when the energy is deposited in the material by charged particles; among others. *Scintillators* are those luminescent material where the energy is deposited by ionizing radiation (photons, electrons, ions). In this work, we are interested

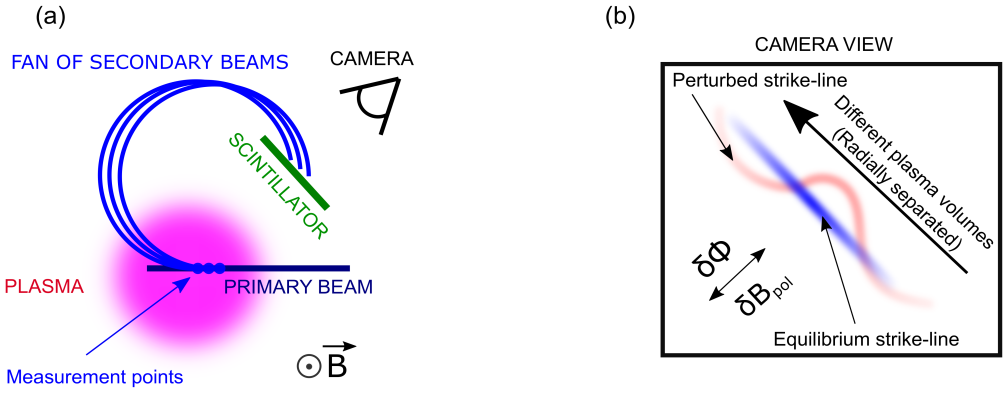

Figure 8: Imaging Heavy Ion Beam Probe (i-HIBP) diagnostic (a) Deflection of secondary beams by magnetic field in the plasma (b) Camera view of the line-shaped trajectory seen on the scintillator by the pass of the secondary beams [13]

in ionoluminescent materials, since they have proven to be truly useful for elaboration of detectors in fusion reactors.

2.1 Principles of Ionoluminescence

Scintillators are normally insulating materials, with a full valence band of bound electrons and an empty conduction band of free electrons. When an ion (for ionoluminescence case) enters the scintillator, it transfers continuously its energy to the atomic electrons of the crystal. These electrons are excited from the valence band to the conduction band. In this excited state, electrons are free to move within the material [14].

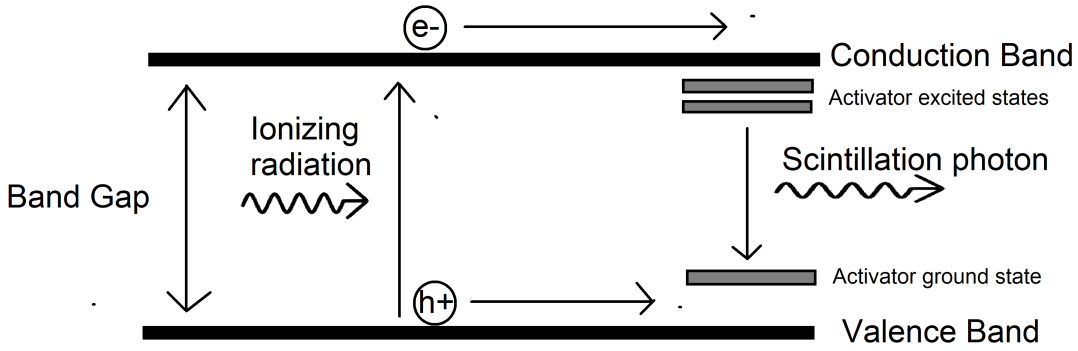

Figure 9: Band structure of a doped scintillator

Straight de-excitations from the conduction band to the valence band are rather unlikely. For this reason, intermediate energy states within the band gap are normally introduced by

impurities in the material. These impurities are called *activators*. Depending on whether these impurities appear naturally in the crystal or are placed by human action (doped), scintillators can be classified in *intrinsic* and *extrinsic*, respectively. Then, as seen in figure 9, promoted electrons move freely within the material until they reach one of these activators. Free electrons are absorbed by the activators, making them reach an excited state. Scintillation photons are then produced in the de-excitation of the activators and are normally within the visible range.

2.2 Theoretical models: Birk-equation

In scintillators, the main factor to be taken into account is the *stopping power* $\frac{dE}{dx}$, which is the energy dE the ion transfers to the crystal when travelled a distance dx. The most widely used model for predictions of light emitted by scintillators is *Birk's model* [15]. The model establishes that the light yield Y of an ion that goes through a scintillator follows the equation:

$$\frac{dY}{dx} = S\frac{dE/dx}{1 + kB \cdot dE/dx}, \tag{5}$$

where dY is the amount of light emitted when the ion travels a distance dx, dE/dx is the stopping power and S and kB are constants specific to each material. Then, the total light Y emitted when the ion has travelled a distance L is:

$$Y = \int_0^L S\frac{dE/dx}{1 + kB \cdot dE/dx}dx. \tag{6}$$

The constant S quantifies the fraction of the deposited energy that is transformed into visible light. There are other processes that compete with the scintillation mechanism explained above [14]. For instance, the electron upon arriving at the impurity site can create an excited configuration that can not transit to the ground state. An additional increment of energy is required then, so the electron raises to a higher-lying state, from which de-excitation to the ground state is possible. One source of this energy is thermal excitation, and the resulting slow component of light is called phosphorescence. It can also happen that, once the electron is captured by the activator, a radiationless transition to the ground state is produced, reducing the light yield. Such processes are called *quenching*.

On the other hand, the inclusion of the constant kB [1], which makes light yield not directly proportional to deposited energy, is related to degradation of the scintillator. Highly ionizing particles (with a high stopping power) might affect the scintillator inner structure on its way through. In the process, so-called *colour centres* might be created. These are regions of the material that absorb radiation with wavelengths within a characteristic interval. So then, scintillation photons can be absorbed without leaving the material and thus reducing the light yield. Hence, how bright a scintillator is depends not only on the

[1] This must not be confused with the Boltzmann constant k_B.

energy the ion carries, but also on the way such an energy is deposited within it.

The constants S and kB must be estimated experimentally for each scintillator. Two limit cases are explored for this purpose:

- For low stopping powers ($kB \cdot dE/dx << 1$):

$$\frac{dY}{dx} \approx S \cdot dE/dx \longrightarrow Y \approx \int_0^L S \cdot \frac{dE}{dx} dx = S \cdot E_{dep}, \tag{7}$$

  where E_{dep} is the total energy deposited in the material. For thick enough samples, the ions will manage to deposit all their energy, so this quantity would be equal to the energy of the incident radiation.

- For high stopping powers ($kB \cdot dE/dx >> 1$):

$$\frac{dY}{dx} \approx \frac{S}{kB} \longrightarrow Y \approx \int_0^L \frac{S}{kB} dx = \frac{S}{kB} L, \tag{8}$$

  where L is the range of the ion within the scintillator.

2.3 Degradation mechanisms

When exposed to large radiation fluxes, scintillators suffer degradation, which normally comes up as a decreasing light yield. This process has mainly three contributions [16]: radiation-induced absorption, where colour centres that absorb the emission photons are created; radiation-induced phosphorescence; and damage to the scintillation mechanism. Due to its longer characteristic time, radiation-induced phosphorescence is seen as a remaining light emission of the scintillator once the incident radiation has ceased. For this reason, this process is also called *afterglow*.

The most common model to predict light yield decrease by degradation is Black-Birk semi-empirical model [17], which relates it to the accumulated fluence F. The accumulated fluence is defined as the quantity of accumulated incident charge (normally in units of amount of ions) per unit of surface of the material. The model establishes that the light yield L follows:

$$L(F) = \frac{L_0}{1 + \frac{F}{F_{1/2}}}, \tag{9}$$

where L_0 the initial not degraded light yield, F the accumulated fluence and $F_{1/2}$ an experimental constant, defined as the fluence necessary to reduce the light yield to half its maximum value. Such a value is characteristic of the scintillator, as well as the radiation species. The model takes into account that molecules in the scintillator are damaged during the irradiation and can absorb the material emission photons, reducing the light yield.

2.4 Scintillator materials: criteria for application in nuclear fusion diagnostics

In order to make the diagnostics discussed above, suitable scintillators must be selected for the conditions of the diagnostics that operate in a tokamak reactor. For this purpose, the main aspects they must fulfil are:

- Peak emission within visible range (380-750 nm).
- Resistance to temperature: in fusion reactors like ITER [8], scintillators might work in temperatures above 500 K, so the selected samples must be able to keep a good yield in this range.
- Fast response: the samples must present a low decay time, in the order of the nanosecond.
- High yield: a high emission rate results in a better signal-noise ratio.
- Low degradation: light yield of scintillators decrease with the accumulated fluence of ions through them. A suitable scintillator must degrade slowly enough, so diagnostics can be carried out without degradation distorting the results.

According to these properties, the following commercial scintillators were selected: TG-Green, ZnS, CSO, YAG and YAGGd. TG-Green is the most widely used scintillator in fusion experiment, due to its fast response and light yield, compared to other scintillators. YAG [18] (Yttrium Aluminium Garnet) is one of the main competitors of TG-Green. It is fast, durable and is widely available, but its light yield is significantly lower than TG-Green. YAGGd is a modification of YAG with Gadolinium. Its advantage with respect

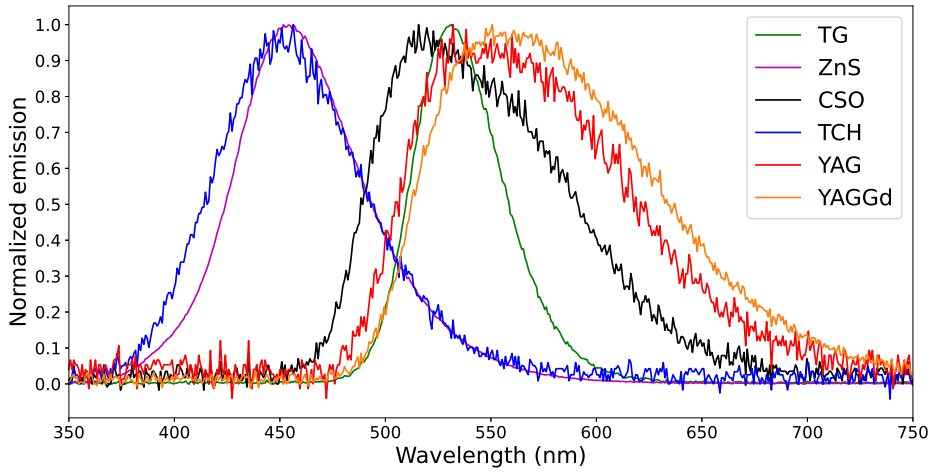

Figure 10: Spectra of scintillator samples at 3 MeV for ^{7}Li, normalized to their maximum values

Figure 11: Centro Nacional de Aceleradores (CNA), at Sevilla

to YAG is a faster response. ZnS [14] is one of the oldest scintillators in the market. This material is most commonly used for alpha detection, for which it has proven to be highly efficient. The main problem with ZnS is that, for thickness greater than about 25 mg/cm^2, it becomes unusable because of the opacity to its own luminescence. CSO [19] is a green phosphor that is more commonly used for fabrication of white LEDS, but that may be also useful for fast ion detection. In addition to the commercial scintillators explained above, a material called TCH (inorganic Ternary Copper Halide) was included [20], which has been developed by the Institute for Nuclear Research (ATOMKI), in Hungary. The parameters of interest are showed in table 1. The emission region is the domain in wavelength within which the scintillator emits light, and its selection is based on the spectra measured during this work. An example is shown in figure 10.

Name	Stoichiometry	λ (nm)	Emission region (nm)	τ (ns)	ρ (g/cm3)
TG-Green	$SrGa_2S_4$:Eu	530	450-650	540	3.65
CSO	$CaSc_2O_4$:Ce	516	450-700	100	-
ZnS	ZnS:Ag	450	350-600	200	4.09
YAG	$Y_3Al_5O_{12}$:Ce	535	450-750	300	4.55
YAGGd	$(Y, Gd)_3Al_5O_{12}$:Ce	570	450-750	106	4.69
TCH	$Cs_3Cu_2I_5$	450	350-600	-	-

Table 1: Selected scintillators for study in this work (characteristics parameters extracted from [18])

3 Experimental setup

All the experiments discussed in this project were carried out at the *Centro Nacional de Aceleradores* [21], at Sevilla (figure 11). All the experiments consisted in measurements of light yield of scintillators when irradiated with ionizing species, under different conditions of energy and current.

3.1 Tandem accelerator

We will focus initially on the tandem-type accelerator used for this work, shown in figure 12. It is a Pelletron 9SDH-2, built by the American National Electrostatic Corporation. A simplified explanation of how it works is exposed below:

1. The negative ions are injected into the tandem with an injection energy $J = eV_{inj}$, where all incoming ions have negative unit charge state.
2. There is a positive electrode in the middle, which accelerates the negative ions to the centre of the accelerator, adding an energy $E_1 = eV_{term}$, where V_{term} is the electrode potential. The charge is accumulated in the electrode via a charging chain and a set of gradient rings homogenizes the electric field. Once the negative ions reach this part, they encounter a stripping chamber filled with a N_2 gas. Here, the ions give up electrons, becoming positive ions with charge state n. More than one type of charge state is produced, since the process is probabilistic.
3. The ions are now positive, so they are ejected by the electrode potential, gaining an energy $E_2 = n \cdot eV_{term}$.

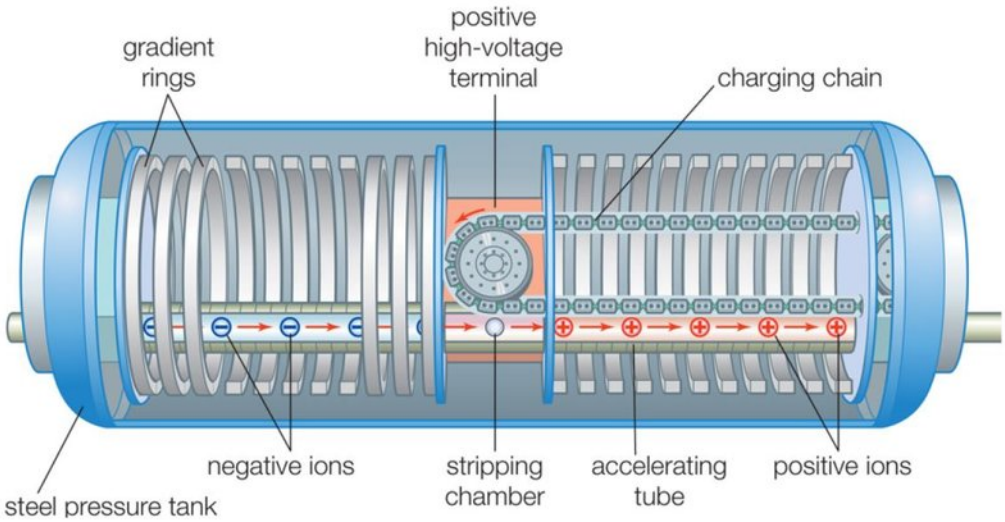

Figure 12: Schematics of tandem-type accelerator [6]

The energy of the outgoing ions is finally:

$$E = J + E_1 + E_2 = eV_{inj} + (n+1)eV_{term} \tag{10}$$

3.2 Acceleration line and measurement setup

The line of the used accelerator is shown in figure 13. The whole process to obtain the desired ion beam consist of the following steps:

1. First, there are three different sources of diverse negative ions: the Alphatross, which produce negative ions from ionized gases; the SNICS, where the ions are results of caesium bombing of solid targets with the desired elements; and the Duoplasmatron, where a gas produces the desired ions due to electric discharges on it. The source employed for this work was SNICS.
2. Then, the negative ions coming from one of the sources reach the tandem accelerator, which mechanism was explained earlier. In this step, positive ions with different energies and charge states leave the tandem.
3. The new positive ions pass through a Wien filter, where an electromagnetic field is applied to select only those ions with the desired energy and charge state. These ions then are deflected by a 90^{o} magnet.
4. Finally, the beam end up in a switching magnet, where they will be redirected to the experimental setup of interest.

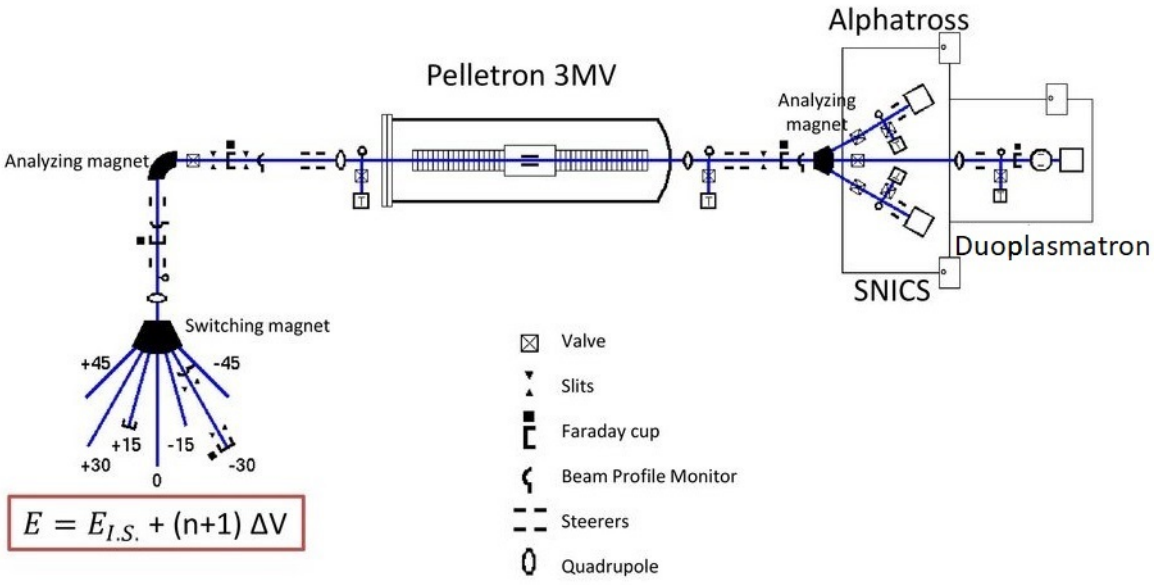

Figure 13: Schematics of acceleration line at Centro Nacional de Aceleradores (CNA), Sevilla [22]

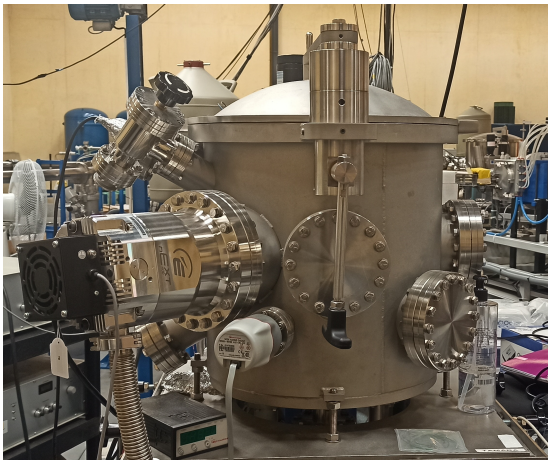

(a) Universal chamber

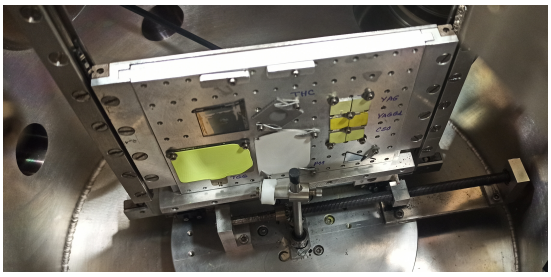

(b) Sample holder

Figure 14: Universal chamber (a) and sample holder (b)

At the end of the acceleration line, it is located the chamber where the scintillators are placed and all the measurements were carried out. It is called *universal chamber*, due to its diverse uses and purposes. It has a primary vacuum pump and a turbo-molecular pump, being able to achieve pressures in the order of 10^{-5} mbar. There is a collimator at its entrance, with an adjustable diameter between 1 and 3 millimetres. The chamber has various windows, in one of which there is a camera attached, which is used to monitor the scintillators in real time. The samples are placed on a rectangular sample holder, which can be moved with stepper motors controlled remotely. Besides, the sample holder itself works as a Faraday Cup and is used to integrate the incident current. The sample holder is connected to a power supply with an adjustable voltage from 0 V to 300 V by 100 V steps. This device is introduced to prevent current measurements to be falsified by the emission of secondary electrons in the sample holder, excited by the ionizing radiation. Both universal chamber and sample holder are shown in figure 33.

The universal chamber has a port for the optic fibre, with a 1 millimetre diameter. The distance between the optic fibre aperture and the sample holder is 22 centimetres. These two lengths determine the solid angle of the optic fibre. The other end of the optic fibre is connected to a spectrometer QEB1478 (as shown in figure 15), which records the spectra. The light that goes into the spectrometer reflects on a collimating mirror and is grated afterwards. The grating is focused then on a CCD detector, that consist of a 2D array of pixels. Each pixel correspond to a wavelength interval and counts are sent by the spectrometer by incident energy unit. The software produces at the end a number of files, each of them being a spectrum of counts per wavelength.

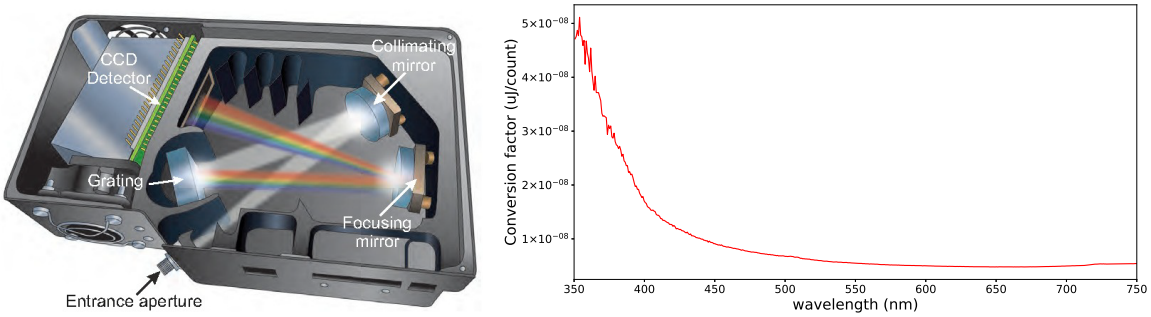

(a) Spectrometer QEB1478 (b) Calibration curve

Figure 15: Spectrometer (a) and calibration curve (b)

3.3 Experimental procedure

The experimental routine carried out for all measurements consist of the following steps:

1. Calibration of spectrometer: the spectrometer must be first calibrated with a well known source, so the spectrum files with counts per wavelength given by the device can be transformed into energy per wavelength. A tungsten halogen lamp (model HL-2000-CAL [23]) with tabulated light yield values was employed to calibrate the optical acquisition system. The obtained calibration curve is shown in figure 15. The spectrometer is connected directly to a PC, where the spectrum files are stored.

2. Adjustment of Wien filter and 90^{o} magnet: depending on the radiation species, charge state and energy of interest, a specific electromagnetic field must be produced in the Wien filter, which is a velocity selector after the tandem exit. The magnetic field in the 90^{o} magnet must be calculated too. This is a necessary step, because more than one type of charge state can be produced in the tandem accelerator. The estimation of such a field is explained in appendix B.

3. Yield measurements: once all the experimental parameters are set, the scintillators light measurements can be started. Prior to measurements at the samples, we make the beam strike the sample holder to measure the actual current, which can be adjusted to the desired value. Then, we make the beam strike the sample on a clean spot (that means, on a non irradiated part). The outputs of the measurements are then: a spectra folder, which contains all the spectra of a sample measured during a shot; and a current file, given by a counter software in a PC connected to the amplifier of the sample holder.

In this work, three different studies were carried out in two sessions, one with ^{7}Li as radiation species and another one with ^{51}V. The studies are:

a) Linearity: the light emission is measured for a current sweep, with the aim to observe linearity of photon rate emission with incident current.

b) Energy scan: for a constant current, the yield of each sample is estimated for an energy sweep of the incident ions.

c) Degradation: the light yield of each sample is measured for longer periods of time, so degradation in the material is clear. The study is made for a constant current and various energies, depending on the radiation species.

4 Analysis and results

4.1 Analysis method

In order to calculate the light yield, The amount of photons emitted by the scintillator [6] must be first estimated. In each spectrum file given by the spectrometer, the number of counts per wavelength $N(\lambda_i)$ is given. These counts can be transformed into energy with the calibration curve $C_{cal}(\lambda_i)$, so the energy spectrum will be:

$$E(\lambda_i) = C_{cal}(\lambda_i) \cdot N(\lambda_i).$$

The energy of a photon with wavelength λ is $E_\gamma = \frac{hc}{\lambda}$. If the spectrum has been integrated with an integration time Δt, the photon rate that reach the optic fibre is then:

$$N_\gamma^{OF}(\lambda_i) = \frac{E(\lambda_i)}{\Delta t \cdot hc/\lambda_i} = \frac{C_{cal}(\lambda_i) \cdot N(\lambda_i)}{\Delta t \cdot hc}\lambda_i.$$

If an isotropic photon emission of the sample is assumed, then the fraction of photons that reach the optic fibre is :

$$N_\gamma^{OF}(\lambda_i) = \frac{\Omega}{4\pi}\Gamma_\gamma(\lambda_i),$$

where Ω is the solid angle of the aperture of the optic fibre and $\Gamma_\gamma(\lambda)$ the photons emitted by the sample. In the universal chamber, the distance between the optic fibre aperture and the sample holder is $d = 22$ cm and the optic fibre has a diameter $\Phi \approx 1$ mm. The solid angle is then:

$$\frac{4\pi}{\Omega} = \frac{4\pi d^2}{\pi \cdot (\Phi/2)^2} = 7,744 \cdot 10^5 \longrightarrow \epsilon_{geom} = \frac{\Omega}{4\pi} = \frac{1}{1.744} \cdot 10^{-5} = 1.29 \cdot 10^{-6},$$

where ϵ_{geom} is the geometric efficiency of the acquisition system. Finally, the Region Of Interest (ROI) $[\lambda_1, \lambda_2]$ is defined, within which the emission spectrum is found. This corresponds to the emission region shown in table 1. The total photon rate is then the integration within this interval:

$$\Gamma_\gamma = \sum_{\lambda_i \in ROI} \frac{4\pi \cdot C_{cal}(\lambda_i) \cdot N(\lambda_i)}{\Omega \cdot \Delta t \cdot hc}\lambda_i = \frac{4\pi}{\Omega \cdot hc \cdot \Delta t} \sum_{\lambda_i \in ROI} C_{cal}(\lambda_i) \cdot N(\lambda_i). \qquad (11)$$

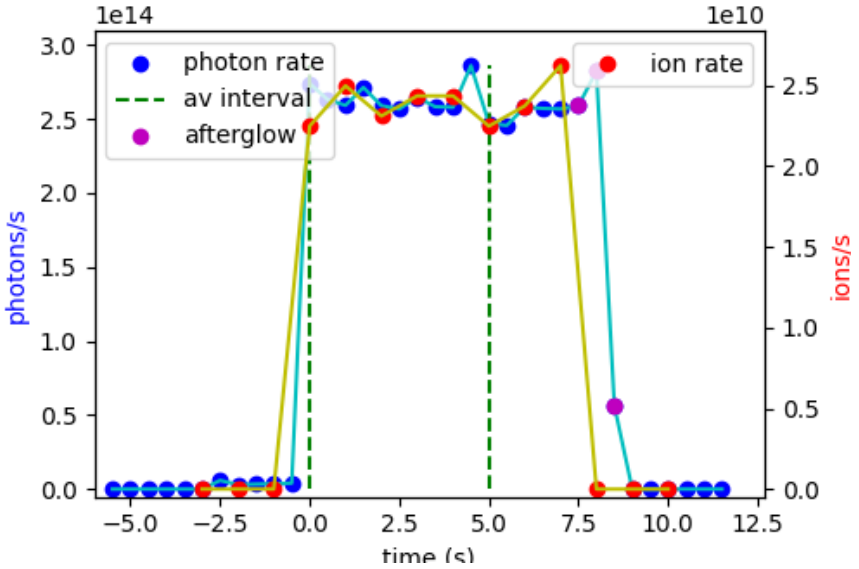

Figure 16: Example of photon rate curve (blue points) and ion current curve (red points) obtained from analysis routine. Those emission points corresponding to afterglow are highlighted in purple

Once the process is completed, a spectrum is transformed into a Γ_γ value. On the other hand, the current file is easily transformed into ions per unit of time as

$$I_{ion}(t) = \frac{I_A(t)}{n \cdot e \cdot \Delta t_{current}},$$

where n is the charge state and $\Delta t_{current}$ the current integration time, fixed at 1 second. The outputs of this routine are a photon rate curve and an ion rate curve, like those shown in the example of figure 16. To estimate the absolute yield ϵ, an *average interval* $[t_1, t_2]$ is to be selected. The yield is estimated then as the ratio between the average photon rate and the average ion rate within the interval:

$$\epsilon = \frac{\overline{\Gamma}_\gamma}{\overline{I}_{ion}} = \frac{\frac{1}{N_\gamma}\sum_{t_1}^{t_2}\Gamma_\gamma(t)}{\frac{1}{N_{ion}}\sum_{t_1}^{t_2} I_{ion}(t)},$$

where N_γ and N_{ion} are the number of points taken from the photon rate and ion rate curve, respectively. The uncertainty of the absolute yield is estimated via uncertainty propagation from those of the mean photon rate and the mean ion rate.

4.2 SRIM simulations

Aiming to know how much energy would the employed radiation species deposit on the samples, a series of simulations in SRIM [24] (Stopping and Range of Ions) were carried

out. SRIM is a software for calculations related to interactions between ions and matter. With these simulations, both the projected range and the stopping power of the ions used in this work were estimated for energies from 0 to 4 MeV.

The estimated stopping powers are plotted in figures 17 and 18 for lithium and vanadium as radiation species, respectively. TCH and CSO were excluded because their exact densities were unknown, so no precise stopping power could be estimated. It is shown in the graph that ^{51}V is clearly more ionizing than ^{7}Li, since its stopping power is larger in all cases. The difference in shape between ^{7}Li and ^{51}V is due to the fact that stopping power has two contributions, depending on the type of interaction between the ion and the material: nuclear (with nuclei of the atoms that conform the scintillator) and electronic (with electrons of the atoms). Hence, the total mean stopping power $\left\langle \frac{dE}{dx} \right\rangle$ can be described as:

$$\left\langle \frac{dE}{dx} \right\rangle = \left\langle \frac{dE}{dx} \right\rangle_{el} + \left\langle \frac{dE}{dx} \right\rangle_{Nucl} \tag{12}$$

Mean values must be taken in equation 12, because energy loss is a probabilistic process and the exact values may change from case to case. Nuclear stopping power is relevant only at low energies, and its value increases with atomic number [14]. Therefore, its contribution in ^{51}V is much higher than in ^{7}Li, resulting in the shape difference at low energies. Since projected range strictly increases with energy, the projected range and

	TG-Green	ZnS	YAG	YAGGd	CSO	TCH
Projected range Li (um)	5.92	5.53	4.08	5.2	8.55	6.59
Lateral straggling Li (um)	0.54	0.52	0.32	0.53	0.59	0.82
Projected range V (um)	1.76	1.6	1.34	1.63	2.98	1.94
Lateral straggling V (um)	0.35	0.30	0.22	0.35	0.44	0.52

Table 2: Projected range and lateral straggling of lithium and vanadium ions at 3 MeV

lateral straggling at 3 MeV for both species were calculated too. The results are shown in table 2, where, for CSO and TCH, approximated densities given by the program were included for a qualitative picture. All the samples handled during the experiments are at least 10 μm thick. While ranges in vanadium are much lower than this range, the same cannot be said for lithium. Since projected range is a mean value, there may be ^{7}Li ions that leave the material without depositing all their energy. This factor must be considered for the following results. Regarding the lateral straggling, the deposited sample areas were in the order of the centimetre. The distances between the selected clean spots on each scintillator were then in the order of tens of millimetres. Therefore, degradation issues due to lateral spreading of damaged molecules should not be significant.

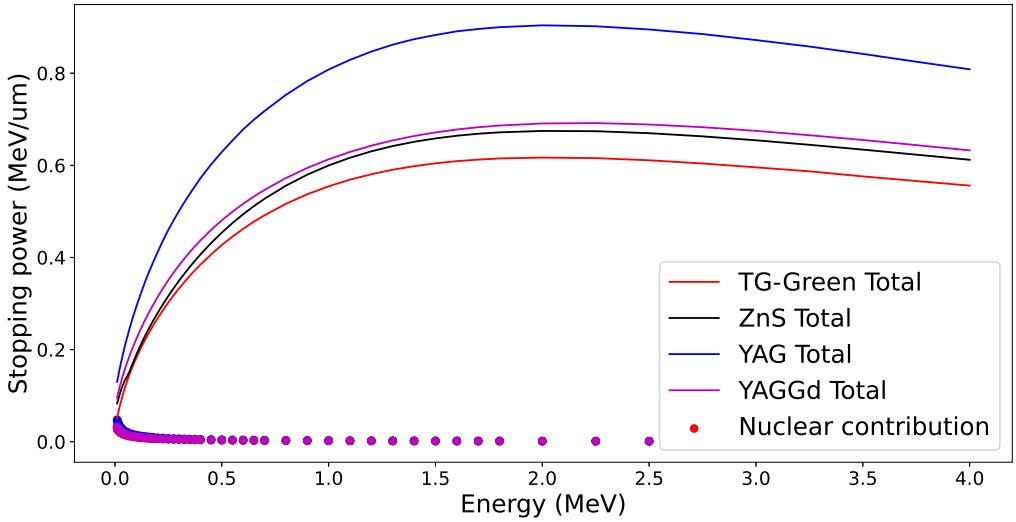

Figure 17: Stopping power as a function of energy for ^{7}Li as radiation species, estimated with SRIM.

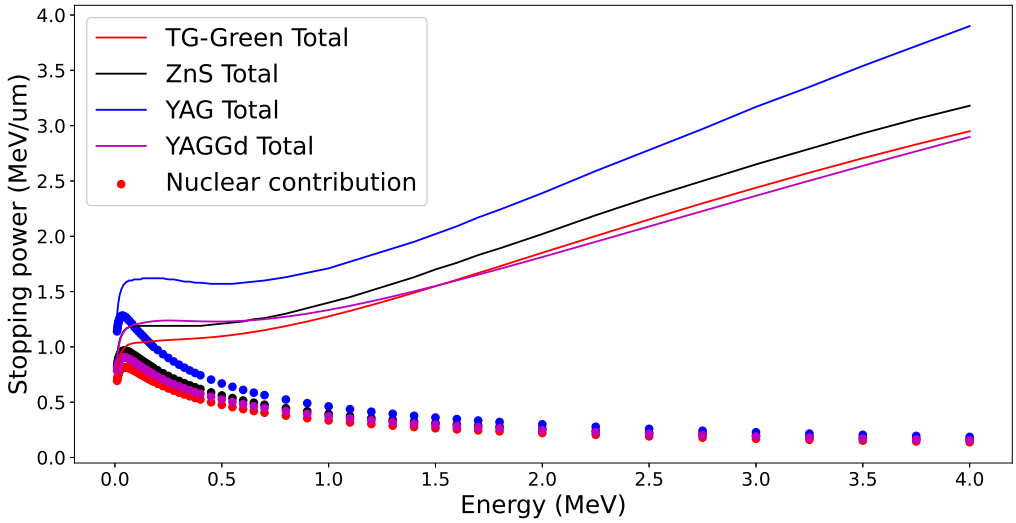

Figure 18: Stopping power as a function of energy for ^{51}V as radiation species, estimated with SRIM.

4.3 Characterization of current measurement

During the experiments with lithium, the currents measured in the samples were in some cases higher than those measured in the sample holder. A possible explanation might be the emission of secondary electrons in the sample holder, due to a non-enough high suppression voltage. Besides, arcing was observed in the currents measured in the samples, similar to a condenser discharge. They may be a result of a not adequate electrical contact of the samples to the holder.

In order to verify this possibility, the current measured in the samples was measured for sweep of the suppression voltage for discrete values of 0 V,100 V, 200 V and 300 V. The results are plotted in figure 19. It can be seen that, indeed, current integrated by the Faraday Cup is higher for lower suppression voltages for all samples. Therefore, it seems that the current measurements were affected by secondary electron emissions. Nevertheless, the only significant case is TCH. In this case, current actually appears to decrease for lower eV-Voltage (until 100 V). Then, for a suppression voltage of 0 V, measured current increases quickly up to 20 nA.

For both ^{7}Li and ^{51}V, the current measurement in the sample and the closest current measurement in the sample holder were compared during the energy scan. The ratio between these two current measurements is shown in figures 20 and 21 for lithium and vanadium, respectively. In the first case, the current measured in the sample holder remain in the region of 75%-125% of that measured in the sample for energies up to 3 MeV for all the scintillators, except TCH. Such deviations may be explained by current fluctuations. , so the use of the current measurement in the sample is justified. However, current measurements in TCH are more than 50% lower than those in the sample holder for energies of 2.5

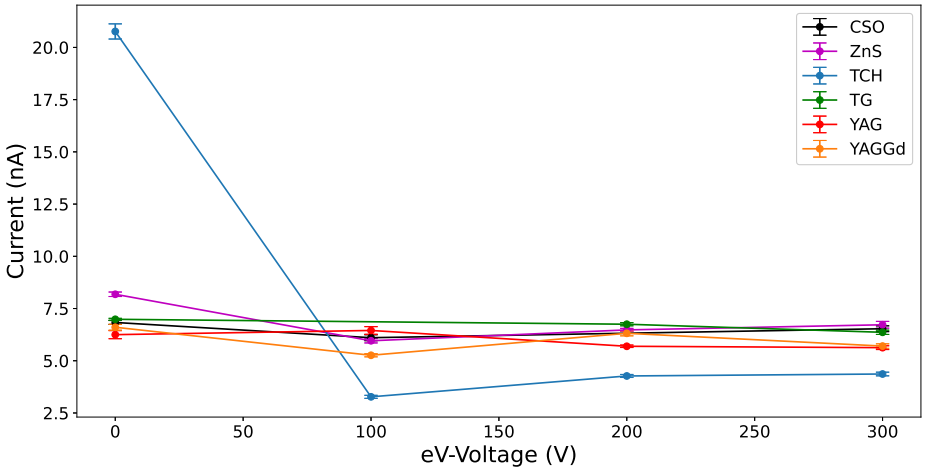

Figure 19: Current vs eV-Suppression voltage for 2 MeV

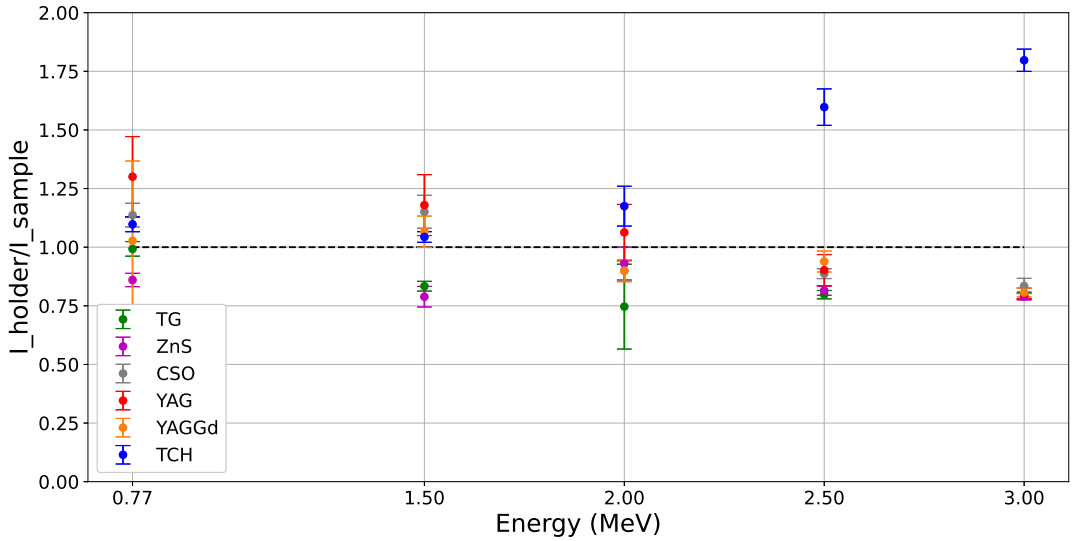

Figure 20: Ratio between current measured in the sample holder and current measured in the sample as a function of ion energy for ^{7}Li as radiation species

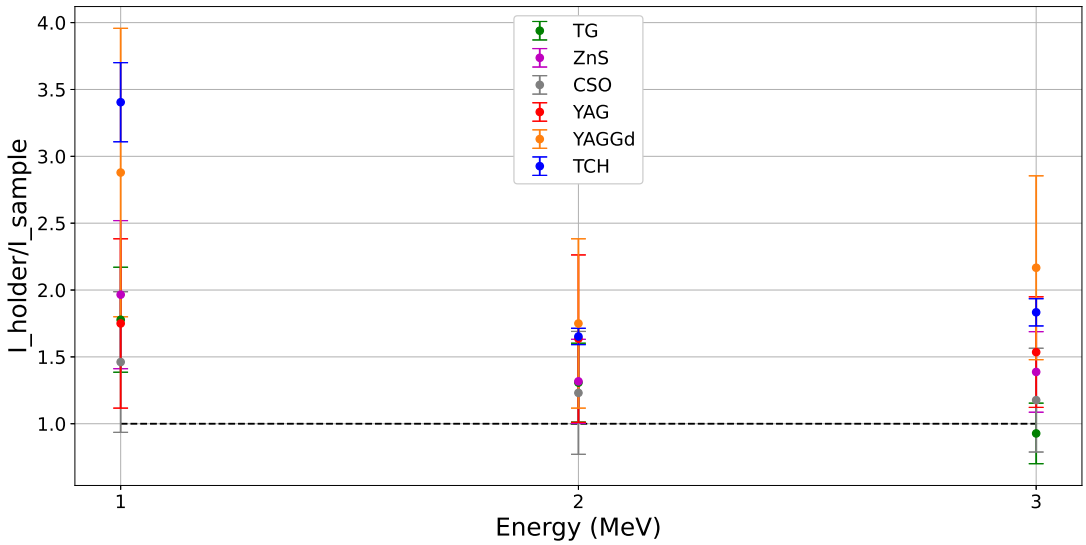

Figure 21: Ratio between current measured in the sample holder and the sample as a function of energy for ^{51}V as radiation species

and 3 MeV. In this case, TCH light yield was also estimated with the current measured in the sample holder for better accuracy.

In ^{51}V case, current measurements in the sample holder were always higher than those in the samples. The most isolating materials were TCH and YAGGd, while TG-Green and CSO presented the lowest deviations between measurements in the holder and the sample. Besides, the ratio between the two measurements is significantly higher with vanadium (TCH presents ratios up to 3) than with lithium (the highest ratio is 1.75). Therefore, it seems that the scintillators are more insulating to ^{51}V than to ^{7}Li. For this reason, only the currents measurements in the sample holder were taken into account for yield estimations with ^{51}V.

4.4 Experiments with ^{7}Li

In the linearity study with ^{7}Li, the current sweep was carried out from 5 nA to 30 nA with 5 nA steps for 1 MeV energy and +1 charge state. The recorded photon rates are shown in figure 22. ZnS was excluded from the study due to its fast degradation. During the whole session, notable degradation was suffered by all samples. Photon rate values used for linearity and energy scan are those corresponding to the peak emission, when degradation is the lowest. However, due to the high current reached here, ZnS degraded so fast that no realistic emission could be used.

As seen in figure 22, a linear dependence with current is seen. Hence, it seems that, at least for the currents handled here, the ratio of photons per unit of current is independent of the amount of current itself (except for degradation). If a linear regression is applied, the light yield can be estimated by taking the slope. The fit results are in table 3. TG-

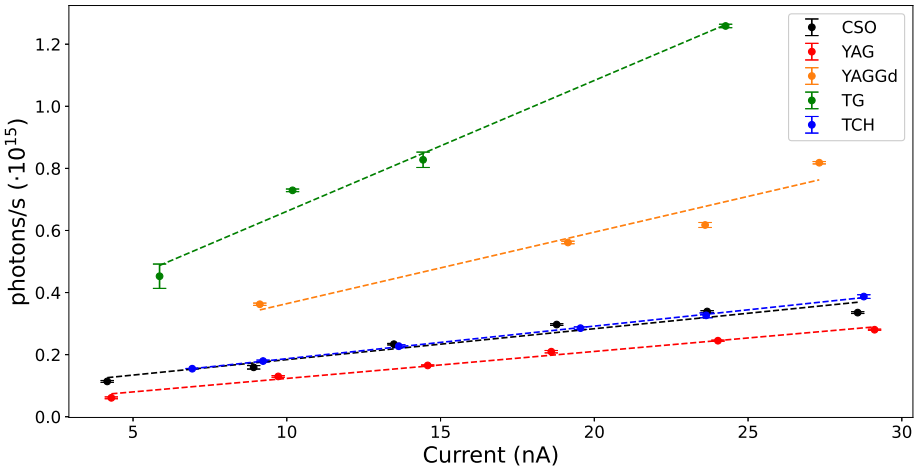

Figure 22: Photon rate emission vs ion current for ^{7}Li at 1 MeV

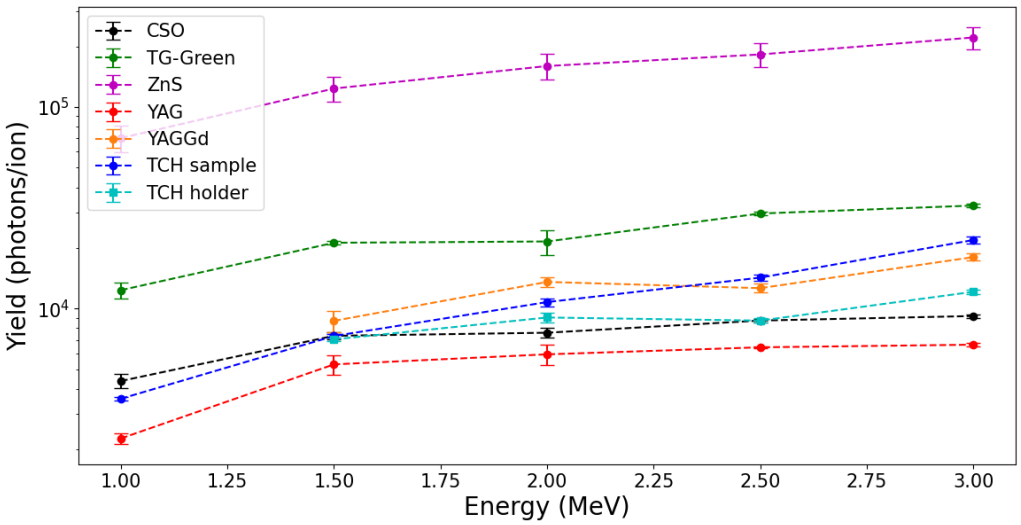

Figure 23: Yield vs Energy for ^{7}Li as radiation species and charge state +1

Green is the brightest sample, followed by YAGGd, TCH, CSO and finally YAG. The uncertainties are those given by the linear regression.

Sample	TG	CSO	TCH	YAG	YAGGd
Yield (photons/ion)	6700 ± 600	1590 ± 200	1679 ± 23	1390 ± 80	3700 ± 700
r^2	0.98	0.94	0.9993	0.99	0.93

Table 3: Yield extracted from linearity study for ^{7}Li at 1 MeV

The energy scan was carried out for an energy sweep from 1 MeV to 3 MeV with a constant current of 5 nA and charge state +1. The results are plotted in figure 23 and are qualitatively similar to what we saw in the linearity study, except that now ZnS was measured too. ZnS present a much higher yield than all the other samples, and this difference increases with energy. The specific values of the yield are in table 4 and let us have a picture of which scintillators are more efficient in general. For all energies, ZnS is the brightest material, followed by TG-Green, YAGGd, TCH, CSO and finally YAG.

For the degradation study with ^{7}Li, the light yield was measured for 2 and 2.5 MeV at current of 5 nA and charge state +1. To quantify the rate of degradation, the decrease of the normalized emission I/I_o (photon rate emission by its maximum value, which is normally the first one) with the accumulated fluence F was observed. Since the diameter of the collimator is 3 mm, the area of impact is $A = \frac{\pi \cdot 0.3^2}{4}\,\mathrm{cm}^2 = 0.0707\,\mathrm{cm}^2$. The

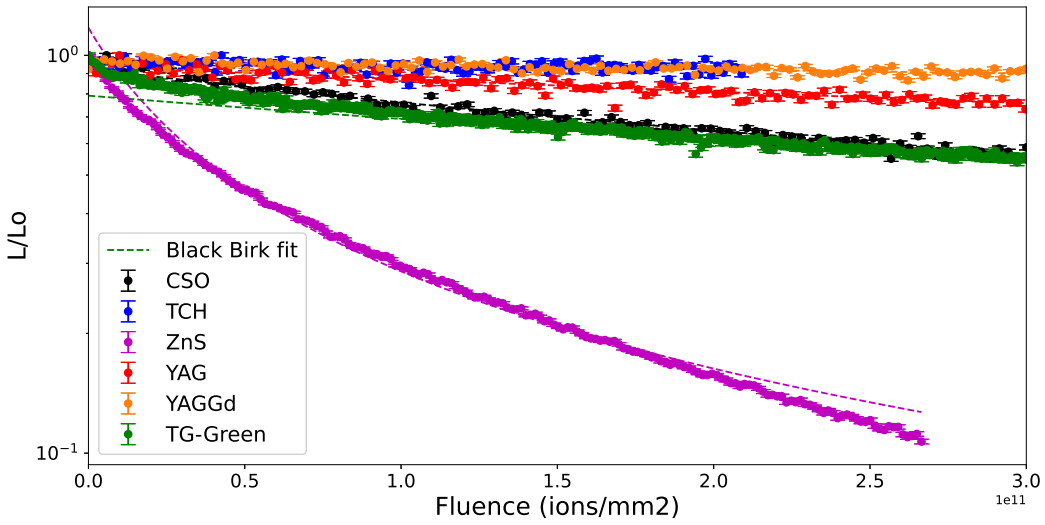

Figure 24: Normalized emission rate as function of fluence at 2.5 MeV for ^{7}Li

accumulated fluence at an instant t' is then:

$$F = \sum_{t=t_o}^{t=t'} \frac{I_{ion}(t)}{A},$$

where t_0 is the instant of peak emission. The results for 2.5 MeV are plotted in figure 24. By just looking at the graph, it is clear that the material that degrades the most is ZnS, followed by TG-Green, CSO, YAG, YAGGd and finally TCH. This is the main drawback of ZnS. Even though its peak emission is much larger than other samples, it degrades much faster, so its lifetime is much shorter. The same order is observed for 2.5 MeV.

Yield ($\cdot 10^3$ photons/ion)

Energy (MeV)	TG	CSO	ZnS	TCH	YAG	YAGGd
1	12.4 ± 1.1	4.4 ± 0.4	70 ± 11	3.57 ± 0.08	2.2 ± 0.13	8.7 ± 1.1
1.5	21.2 ± 0.5	7.3 ± 0.3	124 ± 17	7.32 ± 0.15	5.3 ± 0.6	13.6 ± 0.7
2	22 ± 3	7.6 ± 0.4	160 ± 23	10.8 ± 0.5	5.9 ± 0.7	12.6 ± 0.6
2.5	29.6 ± 0.6	8.73 ± 0.18	182 ± 24	14.3.0 ± 0.5	6.43 ± 0.05	18.0 ± 0.7
3	32.5 ± 0.7	9.19 ± 0.17	220 ± 3	21.9 ± 0.8	6.63 ± 0.11	17.3 ± 0.4

Table 4: Energy scan at 5nA with ^{7}Li

In order to verify the Black-Birk model 9, the results were fitted to obtain the fluence of 50% $F_{1/2}$. More specifically, it was made a linear regression of $\frac{L_0}{L} - 1$ with respect to F. The results of the linear regression are in table 5 confirm what was seen in figure 24. The uncertainties are those given by the linear regression. For all samples (except

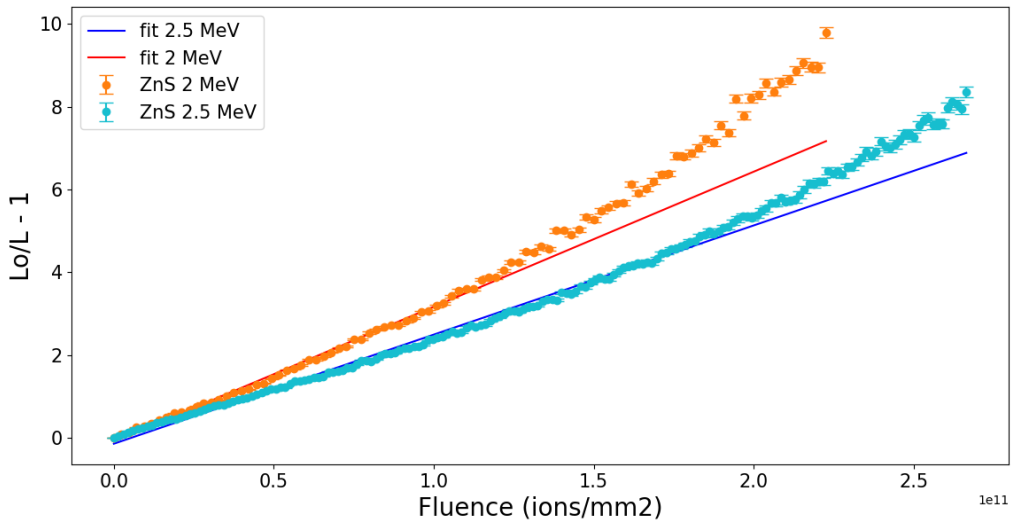

Figure 25: Normalized glow of ZnS as a function of accumulated fluence

YAG), degradation rate seems to decrease at higher energies, being necessary a larger accumulated fluence to reach the same reduction of yield. Values for TCH and YAGGd are less accurate due to low degradation suffered by these two samples. Nevertheless, low degradation is still an advantage with respect to the other materials.

$F_{1/2} \cdot 10^{12}(ions/cm^2)$

Energy	TG	CSO	ZnS	TCH	YAG	YAGGd
2 MeV	48.7 ± 0.9	37.2 ± 0.9	3.06 ± 0.03	300 ± 40	198 ± 18	274 ± 21
2.5 MeV	54.84 ± 0.20	43.1 ± 0.4	3.789 ± 0.025	680 ± 230	117 ± 3	400 ± 30

Table 5: $F_{1/2}$ for 2 and 2.5 MeV with ^{7}Li as radiation species

In general, the experimental results followed the Black-Birk model properly, with a linear dependence of the normalized light emission L/L_0 on the fluence F. However, a deviation from the model was observed in ZnS for both 2 and 2.5 MeV. As seen in figure 25, for large accumulated fluences, the normalized glow is lower than what Black-Birk model predicts. That is to say, ZnS degrades faster at high accumulated fluences than what predicted by the model.

4.5 Experiments with ^{51}V

For the linearity study, only TCH and TG-Green were measured at 1 MeV with currents of 5, 10 and 13 nA and at 3 MeV with currents of 5, 10 and 15 nA. The measurements were carried out at the end of the campaign with already degraded samples. This way,

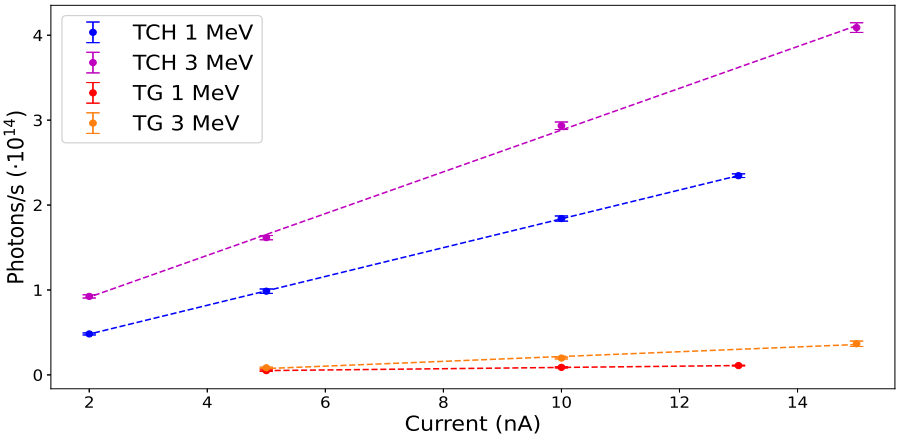

Figure 26: Photon rate vs current with ^{51}V as radiation species

more accurate results may be obtained and the degree of total degradation of the samples is noted. No higher current values could be achieved stable enough for ^{51}V. As seen in figure 26, clear linearity is followed for ^{51}V as well. The yields estimated from the slope of the linear regression are in table 6.

Yield ($\cdot 10^3$ photons/ion)

Energy (MeV)	TG-Green	TCH	r^2 TG-Green	r^2 TCH
1	0.119 ± 0.003	2.719 ± 0.007	0.9995	0.99999
3	0.45 ± 0.05	3.94 ± 0.08	0.99	0.9992

Table 6: Yield extracted form linearity study for ^{51}V

The energy scan was conducted for 0.83 MeV and from 1 MeV to 3 MeV with 0.5 MeV steps, with a current of 2 nA and charge state +1 for 1 and 1.5 MeV and +2 for the rest (due to current stability issues). As seen in Figure 27, the relative glow of the sample remain the same way as for ^{7}Li. ZnS is the brightest material, followed by TG-Green, YAGGd, CSO, TCH and YAG.

Yield ($\cdot 10^3$ photons/ion)

Energy (MeV)	TG-Green	CSO	ZnS	TCH	YAG	YAGGd
0.83	6.3 ± 1.4	1.3 ± 0.3	1.8 ± 0.4	2.8 ± 0.6	1.9 ± 0.4	4.8 ± 1.1
1	8.0 ± 1.7	4.0 ± 0.9	29.0 ± 7.0)	5.5 ± 1.3	3.6 ± 0.8	10.1 ± 2.3
1.5	24.6 ± 2.1	6.8 ± 1.5	22.0 ± 5.0	6.6 ± 1.5	5.6 ± 1.1	15.0 ± 3.0
2	45 ± 10	8.8 ± 2.2	93 ± 22	9.1 ± 0.4	8.0 ± 1.9	14.0 ± 3.0
2.5	48 ± 10	9.8 ± 2.2	120 ± 30	12.4 ± 0.5	8.99 ± 0.10	22.8 ± 0.5
3	51 ± 12	13.0 ± 3.0	200 ± 40	15.4 ± 0.4	10.7 ± 0.4	21.3 ± 0.6

Table 7: Energy Scan with 2 nA of ^{51}V

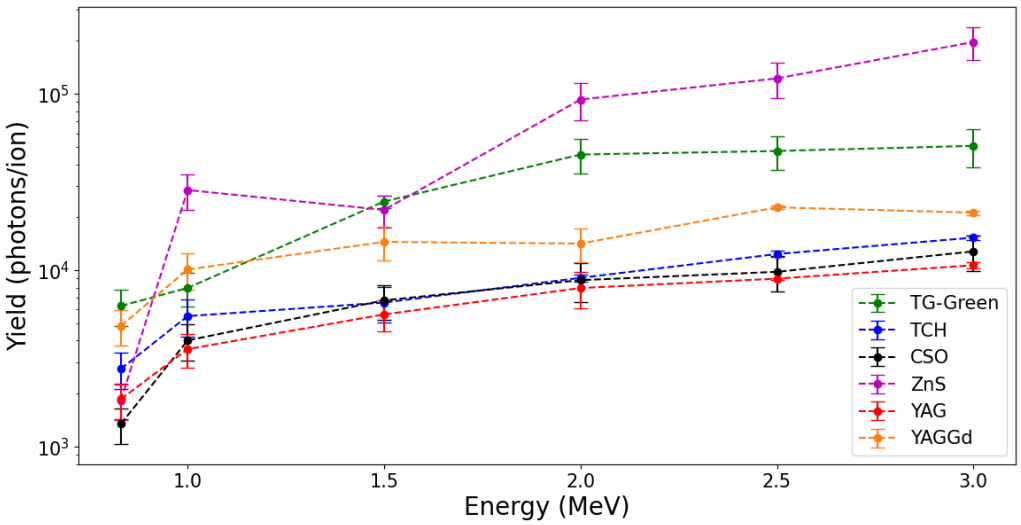

Figure 27: Energy Scan with 2 nA of ^{51}V

The specific yield values are in table 7. In most cases, only the first emission point was taken into account, due to fast degradation of the samples with ^{51}V. This aspect make the estimated yield less accurate than with ^{7}Li.

For the degradation study, the normalized emission rate is plotted in figure 28. Like in the case of ^{7}Li, the fastest degrading material is ZnS, followed by TG-Green, CSO, YAGGd, YAG and TCH. However, the normalized glow curves follow the shape of those with ^{7}Li, but with an accumulated fluence of the order 10^{10} ions/cm^2, instead of 10^{12} ions/cm^2. Hence, the degradation with ^{51}V is much faster. Like in the first session with ^{7}Li, the degradation results were fitted to Black-Birk's model in order to estimate $F_{1/2}$. The values obtained are registered in table 8.

F1/2 ($\cdot 10^{10}$ ions/cm2)

Energy	CSO	TCH	ZnS	YAG	YAGGd	TGreen
1 MeV	42.4 ± 1.5	1680 ± 230	6.42 ± 0.17	132 ± 12	151 ± 7	50.1 ± 0.7
2 MeV	45 ± 4	1040 ± 150	3.53 ± 0.11	213 ± 17	215 ± 6	42.9 ± 0.5
3 MeV	40.8 ± 1.4	1510 ± 120	3.31 ± 0.8	213 ± 5	295 ± 5	44.9 ± 0.4

Table 8: $F_{1/2}$ for ^{51}V as radiation species.

All samples followed Black-Birk's model accordingly, as shown in figure 28.

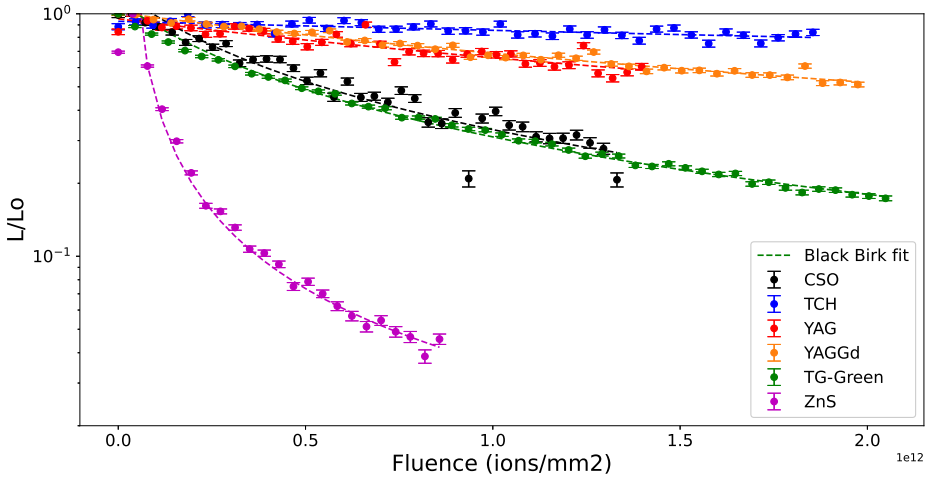

Figure 28: Normalized emission vs fluence at 2 MeV for ^{51}V as radiation species

4.6 Application of Birk's model

We are interested in checking whether the Birk-model 5 is fulfilled by the samples for the species used in this work (Li and V). For the energies handled in this work, The limit for high stopping powers ($dE/dx >> 1/kB$) was applied. In this limit, it is fulfilled:

$$Y \approx \frac{S}{k} \cdot L,$$

where Y is the light yield and L the projected range of the ion within the sample. Therefore, if the light yield estimated in the energy scan is plotted versus the projected range associated with their energy, the ratio S/k can be calculated by making a linear regression. The projected range was estimated via simulations in SRIM. Since the projected range depends on the density of the sample and no accurate density values for CSO and TCH were available, they were excluded for this study. The linear regression carried out in the rest of samples is shown in figure 29 and the corresponding S/k constants are in table 9.

Constant S/k ($\cdot 10^3$ photons/(ion $\cdot \mu$m))

Sample	Li	r^2 Li	V	r^2 V
TG-Green	6.0 ± 0.8	0.944	43 ± 8	0.92
ZnS	48 ± 4	0.98	180 ± 40	0.87
YAG	1.8 ± 0.5	0.78	8.8 ± 0.4	0.994
YAGGd	3.0 ± 0.8	0.83	12 ± 3	0.836

Table 9: Constant S/k estimated from linear regression of light yield vs projected range

In principle, yields from both Li and V should be correlated by the same straight line,

since Birk's model establishes that light yield depends only on stopping power of the ion and not the species itself. This assumption is motivated by its achieved success in previous works [25] [6]. However, as seen in figure 29, light yields corresponding to vanadium are far from correlating to those of lithium. In fact, regressions for vanadium case give systematically higher values for S/k. Nevertheless, it must be considered that yields estimated for vanadium are more affected by issues like degradation, which hinder the calculations.

Both experimental yields and yields predicted by Birk's fit were also plotted in figures 30 and 31 for lithium and vanadium case, respectively. For lithium, all the fitted values are within the experimental error. In the vanadium case, YAG, YAGGd and TG-Green follow nicely the adjusted values, while ZnS presents a strong deviation from the model at 1 MeV. This deviation could be explained by the abnormally high light yield of ZnS at this energy. This can be clearly seen in table 7, where ZnS presents a higher light yield for 1 MeV than for 1.5 MeV, contrary to the case for all other samples. One possible explanation might be that, due to the fast degradation of ZnS, the estimated light yields for higher energies were more degraded. This way, the ratio S/kB of ZnS would be higher than what was calculated and the fitted yield value for 1 MeV would be closer to the experimental result.

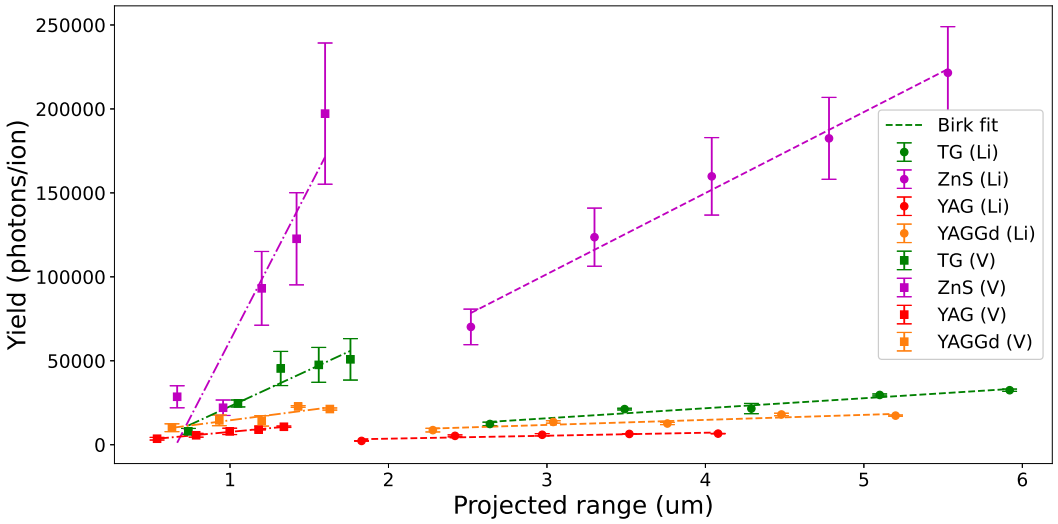

Figure 29: Experimental yields as function of the correspondent projected range for their energies. Round points correspond to lithium, while square points correspond to vanadium. Dashed lines correspond to yield predicted by Birk's model fit

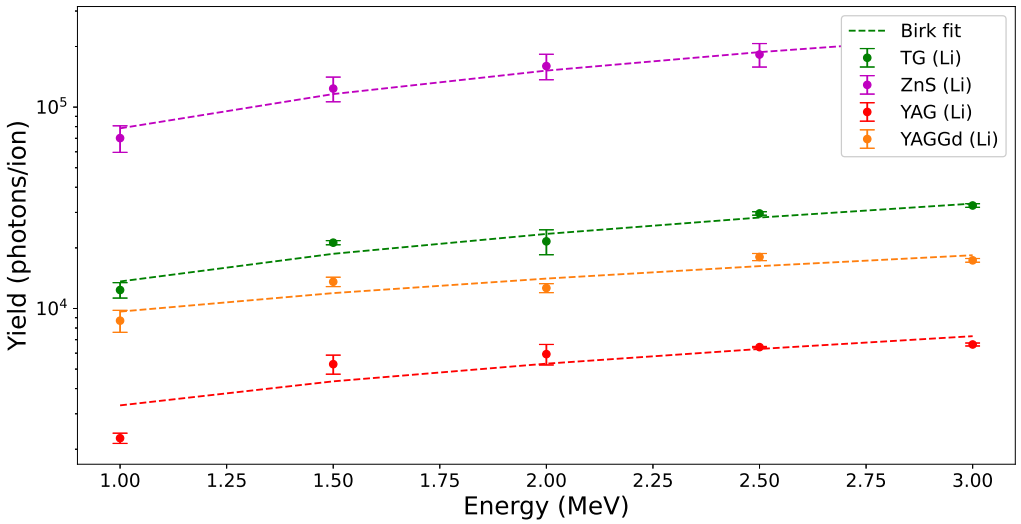

Figure 30: Experimental yields versus energy with Birk's model fit for ^{7}Li as radiation species

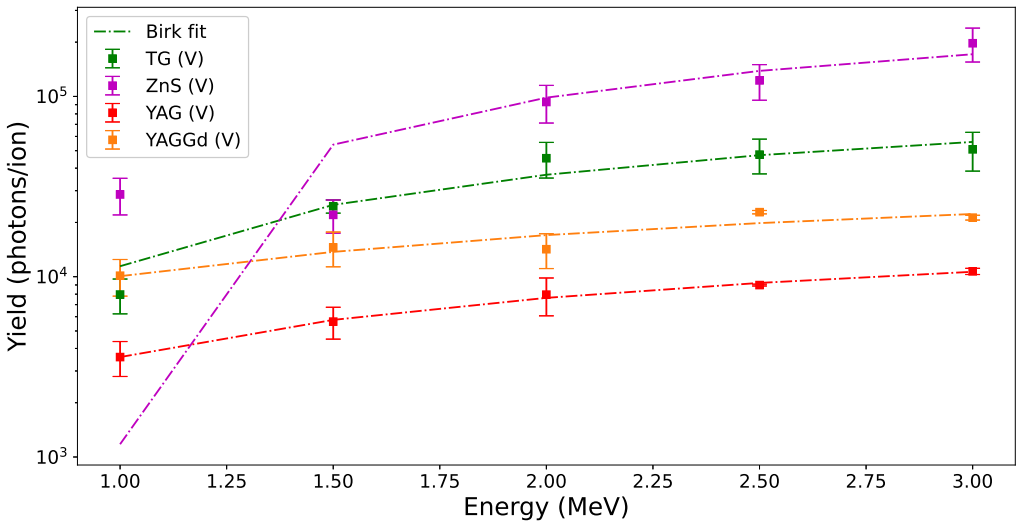

Figure 31: Experimental yields versus energy with Birk's model fit for ^{51}V as radiation species

5 Discussion

5.1 Comparison between ^{51}V and ^{7}Li

The linearity study was motivated by the existence of previous works [26] [27] that proved that photon rate emission is lineal to incident current in TG-Green. It has been proved in this work that, in addition to the TG-Green, all the samples expect ZnS (TCH, CSO, YAG and YAGGd) had a linear response to flux of ^{7}Li ions (figure 22). Besides, TCH also showed linearity for ^{51}V, along with TG-Green. For both radiation species, TCH was the material with the most linear response, with a correlation factor r^2 of 0.9993 for Li and 0.99999 for V. On the other hand, TG-Green is the material with the highest yield extracted from the linear regression, with $(6.7 \pm 0.6) \cdot 10^3$ photons/ion at 1 MeV, followed by YAGGd with $(3.7 \pm 0.7) \cdot 10^3$ photons/ion.

When comparing the energy scan with ^{7}Li and ^{51}V, a pattern is observed. For TG-Green, CSO, YAG and YAGGd, light yield with vanadium at a specific energy is higher than with lithium with the same energy, except at 1 MeV, where the opposite happens. On the other hand, TCH and ZnS show yields always higher with ^{7}Li than with ^{51}V. One possible explanation is the higher projected range of lithium in the materials, as it was shown in table 2. For energies higher than 1 MeV, it might happen that the ions can not deposit all their energy in the scintillator, but transfer just a part and then leave the material. The projected range with vanadium is significantly lower, making this situation less likely. As a consequence, more energy would be deposited by vanadium than by lithium, resulting in a higher light yield. The case of ZnS can be explained by the fast degradation suffered for vanadium. In fact, even the first emission points taken to estimate its yield might be already degraded, resulting in a lower light yield.

In both energy scan and linearity, TCH showed light yields lowers than those estimated by the developers [28]. Experiments in ATOMKI showed that TCH had a higher light yield than materials like GAGG, which is similar to YAGGd. One possible explanation is the substrate where the scintillators were deposited on, which is strainless steel. TCH deposition is optimized for substrates like copper. Deposition in stainless steel is not optimized and the quality of the structure may be hampered.

In the degradation study, it was shown that the fluence of 50% $F_{1/2}$ was two orders of magnitude lower with ^{51}V than with ^{7}Li. Such an aspect could be explained by the difference in stopping power between the two radiation species. When the stopping powers of vanadium and lithium are compared in figures 18 and 31, vanadium have stopping powers much higher than lithium and is thus more ionizing. Therefore, more molecules are damaged by the pass of vanadium and more colour centres are created. Consecutively, a faster creation of these colour centres results in a more decreasing light yield. Besides, the range of ^{51}V within the scintillators is shorter than those of ^{7}Li, so the damage is

more localized. Similar properties have been observed in previous work [6], where, for the same energy, alpha particles degraded faster than protons and deuterium. A quantitative

$F_{1/2}$ ($\cdot 10^{14}$) MeV/cm^2					
M. Rodriguez-Ramos [6]			E. Nieto-Vargas		J. J. Toledo-Garrido [26]
$^{1}H^{+}$	$^{2}D^{+}$	$^{4}He^{++}$	$^{7}Li^{+}$	$^{51}V^{+}$	$^{133}Cs^{+}$
37.00 ± 0.10	9.82 ± 0.17	4.36 ± 0.02	0.974 ± 0.018	0.00501 ± 0.00007	2.970 ± 0.006

Table 10: $F_{1/2}$ of TG-Green comparison for different radiation species

comparison between the obtained values of $F_{1/2}$ of TG-Green in the available literature is shown in table 10. The results of this work seem consistent with those obtained in [6], where ^{7}Li follows the same trend that ^{2}D and ^{4}He. However, the same cannot be said about ^{133}Cs from [26], where the $F_{1/2}$ is extremely higher than that corresponding to ^{51}V. One possible explanation is the range of energies used. The results of this work and [6] were obtained with energies in the range of MeV, while those of [26] were obtained with energies of 55 keV. The stopping power and projected range of ^{133}Cs at 55 keV in TG-Green estimated with SRIM are, respectively, 2,3165 MeV/μm and 0.0271 μm. On the other hand, the same parameters estimated for ^{51}V at 1 MeV are 1,4 MeV/μm and 0,7373 μm. Based on these values, ^{133}Cs at 55 keV is more ionizing than ^{51}V at 1 MeV. The discrepancy might be explained then by the different current densities handled in the two works. For the study with protons, deuterium and alpha particles [6], current densities in the order of 10^{13} ions/cm^{2}s were used, while a current density of around 10^{11} ions/cm^{2}s were handled for ^{51}V during this work (2 nA of +2 charge state ions on an impact area of 0.0707 cm^2). On the other hand, in the study with ^{133}Cs [26], currents densities in the order of 10^{6} ions/cm^{2}s were applied. Hence, there is a difference of five orders of magnitude between the current densities. Besides, M. Rodriguez [6] measurements and ours were carried out in the same experimental setup, at the CNA, while those of J.J. Toledo [27] were done in an i-HIBP injector. In this situation, systematic errors of the experimental setup might be increasing the differences.

5.2 Consistency with Birk's model

Only the limit for high stopping power was applied in this work, motivated by the high energies handled (the lowest one is 1 MeV), along with the use of heavy ions (V and Li) as radiation species. However, this limit alone let us estimate only the ratio S/kB and not their individual values. Nevertheless, this ratio can still be compared to which would be estimated from the constants S and kB calculated in other works. In the available literature [25], values of S and kB were estimated for TG-Green with protons and alpha particles. The ratio of the constants in [25] is $S/kB \approx 15 \cdot 10^3$ γ/(ion $\cdot\mu m$). In this work, we obtained (table 9) values of $(6.0 \pm 0.8) \cdot 10^3$ γ/(ion $\cdot\mu m$) for ^{7}Li and $(43 \pm 8) \cdot 10^3$ γ/(ion $\cdot\mu m$) for ^{51}V. Even though the exact values differ significantly, the order of magnitude is similar. The strong deviation of vanadium case might be explained by degradation issues.

In M. C. Jiménez's paper [25], S has an order of magnitude of 10^5 $\gamma/(\text{ion} \cdot \text{MeV})$ for TG-Green. If we assume (for a qualitative view) that this order of magnitude is shared for all our samples, that would leave $1/kB \sim 10^{-2}$ MeV/μm. On the other hand, for the energies employed to fit Birk's model (1 to 3 MeV), the total stopping power of all the samples would be in the order of MeV/μm (figures 30 and 31). Therefore, there is a difference of two orders of magnitude between the constant kB and the stopping power, making the approached limit of high stopping power suitable.

6 Conclusions

The goal of this work was to characterize scintillators for its use in fusion reactors diagnostics. The selected materials are: TG-Green, ZnS, YAG, YAGGd and TCH. The scintillator samples were irradiated with ^{7}Li and ^{51}V ions with a particle accelerator at the *Centro Nacional de Aceleradores* (CNA), at Sevilla.

Three different studies were carried out: linearity of emission rate with incident ion current; energy scan of light yield; and degradation. In linearity, all the materials (except ZnS, which was excluded) followed the linear relation. The sample with the highest correlation was TCH, with a factor r^2 of 0.9993 for ^{7}Li and 0.99999 for ^{51}V, both at 1 MeV. For the energy scan, ZnS showed the highest light yield, followed by TG-Green, YAGGd, CSO, TCH and YAG. ZnS had a light yield of $(160\pm23)\cdot10^3\,\gamma$/ion for ^{7}Li and $(22\pm22)\cdot10^3\,\gamma$/ion for ^{51}V, both at 2 MeV. In the degradation study, the normalized emission rate was measured with respect to the accumulated fluence. ZnS was the fastest degrading material, followed by TG-Green, CSO, YAGGd, YAG and finally TCH. The results were fitted to Black-Birk's model, which the materials followed accordingly.The estimated factor $F_{1/2}$ for TCH is $(340\pm40)\cdot10^{12}$ ions/cm^2 with ^{7}Li and $(10,4\pm1,5)\cdot10^{12}$ions/cm^2 with ^{51}V. The experimental results were also fitted to Birk's model for the high stopping power limit. All the samples followed nicely the model for ^{7}Li case. The estimated ratio S/kB for TG-Green is $(6,0\pm0,8)\cdot10^3\,\gamma/(\text{ion}\cdot\mu\text{m})$, which share order of magnitude with previous estimations in the available literature. Finally, the case of TCH must be highlighted. It presents the higher linear correlation of emission rate with incident ion rate, which make it a possible candidate for diagnostics like i-HIBP. Despite its low light yield, it is the slowest degrading material of all analysed. This aspect makes it easier to characterize and give it a longer lifetime.

The major limitation during the experiments was the acquisition system, due to the low geometric efficiency, which is in the order of 10^{-6}. As a consequence, for materials like YAG and CSO, the integration time of the spectrometers had to be increased to values in the order of seconds. However, long integration times make the measurements more susceptible to degradation issues. One possible solution is to increase such geometric efficiency, either increasing the optic fibre aperture (with a lens, for example) or making

the distance between the sample holder and the optic fibre shorter. Another limitation was the fixed integration time of the current in the sample holder, which is fixed at one second. This time establishes a minimum to the time passed between two points in the photon rate emission curve when estimating the average light yield. However, for fast degrading materials like ZnS, this time is too long for accurate estimations. This issue could be solved by making changes in the experimental setup, so integration times shorter than one second are possible for current measurements. Lastly, the difference between the current measured in the holder and that measured in the sample made the latter unusable in some cases, hindering the light yield estimation.

Appendices

A Yield calculator software

Due to the high volume of data handled in this work, a software that automates the estimation of the absolute efficiency was developed. The software interface is shown in figure 32. The inputs of the programme are the files obtained in the experiment (spectra folder, current file and calibration curve) plus parameters that depend on the sample (ROI) and those that depend on the incident ions (charge state). When the inputs are processed,

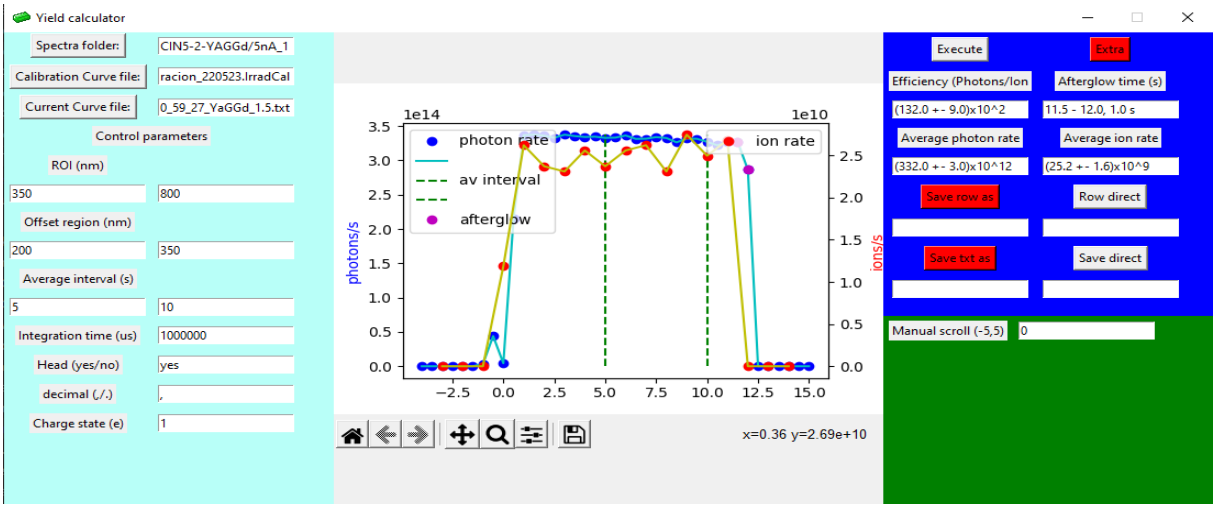

Figure 32: Absolute efficiency calculator software. The directory of the basic files (spectra folder, calibration curve and current file) are introduced on left side, as well as the other experimental parameters (ROI, offset region, charge state, average interval, etc). In the middle centre, a graph with the correlated photon rate curve (blue) and ion rate curve (red) is shown. On the right side, the program returns the estimated yield, average photon rate and average ion rate within the introduced average interval.

the software shows a figure with the correlated photon and ion rate curves as a function of time. The absolute yield is estimated then as the rate between the mean values of both curves within the average interval, set as a control parameter.

In case of afterglow (emission of photons by the scintillators after stop of incident ion beam), the software estimates the time it lasts and the instants when it happens. This is done by taking the instants at when there are non-null photon rate points but null ion rate points, in the tail of the emission curve. Absolute yield, along with the mean photon and ion rate and the control parameters, can be saved as a row in the file. For studies like degradation, there is also an option to export the photon rate curve and the ion rate curve as two text files, both with the associated uncertainties.

B Tandem parameters

At the beginning of each measurement session, a series of experimental parameters must be set in order to obtain the ion beam with the desired energy and charge state. These parameters are:

- TANDEM electrode potential for a molecule case: In the tandem section in this work, the working principle of the accelerator for individual atoms was described. However, sometimes single atoms cannot be extracted from the source, but molecules that contain the desired species. To simplify the equations, we will stick to the simple diatomic molecule case. For this case, the total mass M of the molecule is the sum of the mass m of the desired element and the mas m' of the undesired one. Hence, the energy gained by the molecule in the first half of the accelerator is:

  $$eV_j + eV_{term} = \frac{1}{2}Mv^2 = \frac{1}{2}(m+m')v^2.$$

  The fraction of the total energy corresponding to the desired species up to this point is then:

  $$T = \frac{1}{2}mv^2 = \frac{m}{m+m'} \cdot \frac{1}{2}Mv^2 = \frac{m}{m+m'} \cdot (eV_j + eV_{term}).$$

  Once the molecule pass through the N^2 stripper, the desired species is left alone with charge state n. From here, the process continues as explained in the tandem section. Therefore, the total energy gained by the desired species is:

  $$T = \frac{m}{m+m'} \cdot (eV_j + eV_{term}) + n \cdot eV_{term}.$$

  The result may be extended to more complex molecules by introducing weight coefficients in the $\frac{m}{m+m'}$ factor.

- Wien filter: It is a velocity selector set after the exit of the tandem accelerator. Its purpose is to select only those ions with the desired energy and charge state. Inside

the filter, a constant electric field is set with two metal plates with potential, while a constant magnetic field normal to the electric field is also set with a solenoid. An entering positive ion with charge q and velocity v will feel a force ruled by Lorentz's law:

$$F_q = F_E + F_B = E \cdot q - B \cdot q \cdot v.$$

For the ion to pass through the filter, the net force on it must be null. Hence:

$$0 = E \cdot q - B \cdot q \cdot v \longrightarrow v = \frac{E}{B}.$$

For non-relativistic particles (which are the case in this work), the speed is directly $v = \sqrt{2 \cdot m \cdot T}$. On the other hand, for a short distance d between the charged plates, the electric field may be approximated as $E \approx \frac{\Delta V}{d}$, where ΔV is the applied voltage difference between the plates. The normally variable parameter is the voltage difference ΔV, so it must be estimated as a function of the magnetic field and the energy:

$$v = \sqrt{2 \cdot m \cdot T} = \frac{\Delta V}{d \cdot B} \longrightarrow \Delta V = d \cdot B \cdot \sqrt{2 \cdot m \cdot T}$$

This is the voltage that must be applied in the Wien filter in order to obtain ions with energy T.

- 90^{o} magnet: it is a device inside which a constant magnetic field B is produced to deflect a charged particle trajectory 90^{o}. The magnetic field is set in a way the

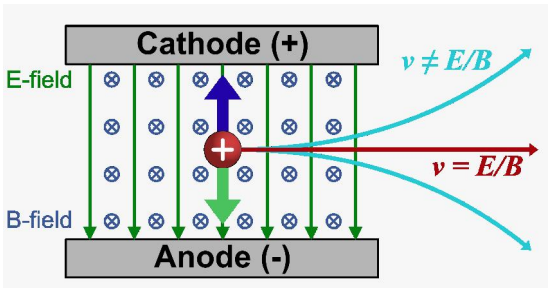

(a) Wien filter. Particles with velocities different from E/B are deflected to the metal plates, while those that fulfil the relation follow a straight line [29]

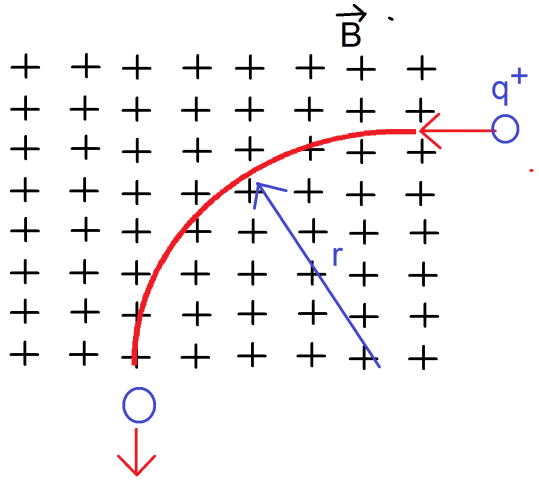

(b) 90^{o} magnet: the charged particle follow a circular trajectory by the influence of the constant magnetic field.

Figure 33: Wien filter (a) and 90^{o} magnet (b) schematics

field lines are normal to the entering particle with charge q and velocity v. Due to Lorentz's law, the particle will follow a circular trajectory of radius r. The compensation between the centripetal and the magnetic force establishes:

$$q \cdot v \cdot B = \frac{m \cdot v^2}{r} \longrightarrow B = \frac{m \cdot v}{q \cdot r} = \frac{1}{r} \cdot \frac{\sqrt{2 \cdot m \cdot T}}{q},$$

where T is the kinetic energy. The radius r is a characteristic parameter of the device and its value is fixed for all cases. Therefore, a suitable magnetic field B must be set so a particle with energy T, mass m and charge q is deflected correctly.

References

[1] *Advantages of fusion*. URL: https://www.iter.org/sci/Fusion.

[2] *Science Made Simple: What Are Nuclear Fusion Reactions?* 2021. URL: https://scitechdaily.com/science-made-simple-what-are-nuclear-fusion-reactions/.

[3] *Nuclear binding energy*. URL: https://phys.libretexts.org/Bookshelves/University_Physics/Book%3A_University_Physics_%28OpenStax%29/University_Physics_III_-_Optics_and_Modern_Physics_%28OpenStax%29/10%3A__Nuclear_Physics/10.03%3A_Nuclear_Binding_Energy.

[4] P. Stott G. McCracken. *Fusion (Second Edition)*. Academic Press, 2012. ISBN: 9780123846563.

[5] A. B. Zylstra; O. A. Hurricane at al. "Burning plasma achieved in inertial fusion". In: *Nature* 601 (2022), pp. 542–548.

[6] M. Rodriguez-Ramos. "Calibración absoluta y aplicación de los detectores de pérdidas de iones rápidos basados en materiales centelleadores para dispositivos de fusión nuclear". PhD thesis. University of Sevilla, 2017.

[7] Y. Xu. "A general comparison between tokamak and stellarator plasmas". In: *Matter and Radiation at Extremes* 1.4 (2016), pp. 192–200.

[8] *ITER*. URL: https://www.iter.org/sci/Goals.

[9] *Max Planck Institute for Plasma Physics: Wendelstein 7-X*. URL: https://www.ipp.mpg.de/w7x.

[10] S. J. Ling; W. Moebs; and J. Sanny. *University Physics, Volume 2*. Samurai Media Limited, 2017. ISBN: 978-9888407613.

[11] J. Galdón-Quiroga et al. "Velocity-space sensitivity and tomography of scintillator-based fast-ion loss detectors". In: *Plasma Physics and Controlled Fusion* 60.10 (2018).

[12] J. Rueda et al. "Design and simulation of an imaging neutral particle analyzer for the ASDEX Upgrade tokamak". In: *Review of Scientific Instruments* 92 (4 2021).

[13] J. Galdón-Quiroga et al. "Conceptual design of a scintillator based Imaging Heavy Ion Beam Probe for the ASDEX Upgrade tokamak". In: *Journal of Instrumentation* 12 (8 2017).

[14] G. F. Knoll. *Radiation Detection and Measurements*. Wiley, 2004. ISBN: 9780470131480.

[15] J. B. Birks. "Scintillations from Organic Crystals: Specific Fluorescence and Relative Response to Different Radiations". In: *Proceedings of the Physical Society. Section A* 64.10 (1951).

[16] C. Kim. "A Review of Inorganic Scintillation Crystals for Extreme Environments". In: *Crystals* 11 (2021), pp. 669–687.

[17] F. A. Black J. B. Birks. "Deterioration of Anthracene under a-Particle Irradiation". In: *Proceedings of the Physical Society. Section A* 64 (1951), pp. 511–512.

[18] M. Videla-Trevin. "Characterization of scintillators for ion detection diagnostics in nuclear fusion reactors". Master's thesis. University of Sevilla, Nov. 2021.

[19] T. Kang et al. "Luminescent properties of CaSc2O4:Ce3+ green phosphor for white LED and its optical simulation". In: *Optical materials* 98.109501 (2019).

[20] M. Hunyadi et al. "Charged-particle induced radioluminescence in nanoclusters of CsPbBr3 perovskite quantum dots". In: *Materials Letters* 289.129398 (2021).

[21] J. Gómez-Camacho et al. "Research facilities and highlights at the Centro Nacional de Aceleradores (CNA)". In: *The European Physical Journal Plus* 136 (2021), pp. 273–288.

[22] *Línea de neutrones en el CNA: HISPANoS (HISPAlis NeutrOn Source)*. URL: `https://slideplayer.com/slide/12259911/`.

[23] *Tungsten Halogen Light Sources*. URL: `https://www.oceaninsight.com/products/light-sources/vis-and-nir-light-sources/tungsten-halogen/`.

[24] *James F. Ziegler - SRIM TRIM*. URL: `http://www.srim.org/`.

[25] M.C. Jiménez-Ramos. "Characterization of scintillator materials for fast-ion loss detectors in nuclear fusion reactors". In: *Nuclear Instruments and Methods in Physics Research B* 332 (2014), pp. 216–219.

[26] J. J. Toledo-Garrido. "Characterization of scintillator screens under irradiation of low energy 133Cs ions". In: *Journal of Instrumentation* 17.P02026 (2022).

[27] J. J. Toledo-Garrido. "Deposición y caracterización de materiales centelladores para su utilización en el detector FILD". Master's thesis. University of Sevilla, 2018.

[28] "M.Hunyadi Private Communication". 2023.

[29] *Centre for exotic nuclear studies: KoBRA Wien Filter Project*. URL: `https://centers.ibs.re.kr/html/cens_en/facilities/infrastructure_0506.html?site_dvs_cd=cens_en&menu_dvs_cd=0506`.